Barotropic tides in the South Atlantic Bight

Brian O. Blanton,[1] Francisco E. Werner,[1] Harvey E. Seim,[1] Richard A. Luettich Jr.,[1] Daniel R. Lynch,[2] Keston W. Smith,[2] George Voulgaris,[3] Frederick M. Bingham,[4] and Francis Way[5]

Received 29 April 2004; revised 12 September 2004; accepted 20 October 2004; published 21 December 2004.

[1] The characteristics of the principal barotropic diurnal and semidiurnal tides are examined for the South Atlantic Bight (SAB) of the eastern United States coast. We combine recent observations from pressure gauges and ADCPs on fixed platforms and additional short-term deployments off the Georgia and South Carolina coasts together with National Ocean Service coastal tidal elevation harmonics. These data have shed light on the regional tidal propagation, particularly off the Georgia/South Carolina coast, which is perforated by a dense estuary/tidal inlet complex (ETIC). We have computed tidal solutions for the western North Atlantic Ocean on two model domains. One includes a first-order representation of the ETIC in the SAB, and the other does not include the ETIC. We find that the ETIC is highly dissipative and affects the regional energy balance of the semidiurnal tides. Nearshore, inner, and midshelf model skill at semidiurnal frequencies is sensitive to the inclusion of the ETIC. The numerical solution that includes the ETIC shows significantly improved skill compared to the solution that does not include the ETIC. For the M_2 constituent, the largest tidal frequency in the SAB, overall amplitude and phase error is reduced from 0.25 m to 0.03 m and 13.8° to 2.8° for coastal observation stations. Similar improvement is shown for midshelf stations. Diurnal tides are relatively unaffected by the ETIC. *INDEX TERMS:* 4219 Oceanography: General: Continental shelf processes; 4255 Oceanography: General: Numerical modeling; 4560 Oceanography: Physical: Surface waves and tides (1255); 4223 Oceanography: General: Descriptive and regional oceanography; *KEYWORDS:* barotropic tide, South Atlantic Bight, finite element model

Citation: Blanton, B. O., F. E. Werner, H. E. Seim, R. A. Luettich Jr., D. R. Lynch, K. W. Smith, G. Voulgaris, F. M. Bingham, and F. Way (2004), Barotropic tides in the South Atlantic Bight, *J. Geophys. Res.*, *109*, C12024, doi:10.1029/2004JC002455.

1. Introduction and Background

[2] The majority of water level variability in many coastal regions is tidal in origin, and a distinct advantage in tidal prediction is that tidal responses occur at discrete frequencies determined by combinations of astronomical frequencies as well as frequencies that result from nonlinear interactions in the governing physics. Harmonic analysis of sufficiently long observations of water level have been used historically for accurate local prediction of tides. However, mapping the spatial character of the tides requires accurate tidal models since observational coverage is generally sparse in the deep ocean. Typical skill in the numerical prediction of M_2 tidal elevation is 0.05 m and 5° (*Foreman et al.* [1995] and *Foreman and Thomson* [1997] on the northwest Pacific coast, *He and Weisberg* [2002] on the west Florida shelf, *Davies and Kwong* [2000] on the northwest European shelf, *Lynch and Naimie* [1993] and *Naimie et al.* [1994] in the Gulf of Maine). However, good tidal skill in the South Atlantic Bight region of the eastern U.S. coast has been comparatively elusive [*Mukai et al.*, 2002].

[3] We present an analysis of observations in the South Atlantic Bight (SAB) that includes recent data from a set of offshore midshelf towers plus an additional mooring in the Grays Reef National Marine Sanctuary (GR) as well as water levels from long-term National Ocean Service (NOS) gauge sites. Depth-averaged velocities are also examined where available. Comparison of numerical model results to the tidal analysis is made, with the goal of determining the best prior estimate of tidal boundary conditions for limited-area model studies [*Lynch et al.*, 2004; *Blanton*, 2003].

[4] The data most routinely available for data-assimilating coastal regional forecasting models are typically from permanent water level gauges in the coastal and nearshore zones. This region can be strongly influenced by tidal inlets and estuaries (as described herein). We have recently shown [*Lynch et al.*, 2004] that assimilation of coastal water level observations must be performed with a model that includes the estuaries and tidal inlets. It is not sufficient to ensure that the landward boundary of the model domain encompasses

[1]Department of Marine Sciences, University of North Carolina at Chapel Hill, Chapel Hill, North Carolina, USA.
[2]Thayer School of Engineering, Dartmouth College, Hanover, New Hampshire, USA.
[3]Department of Geological Sciences, University of South Carolina, Columbia, South Carolina, USA.
[4]Center for Marine Science, University of North Carolina at Wilmington, Wilmington, North Carolina, USA.
[5]Applied Technology and Management, Inc., Charleston, South Carolina, USA.

0148-0227/04/2004JC002455

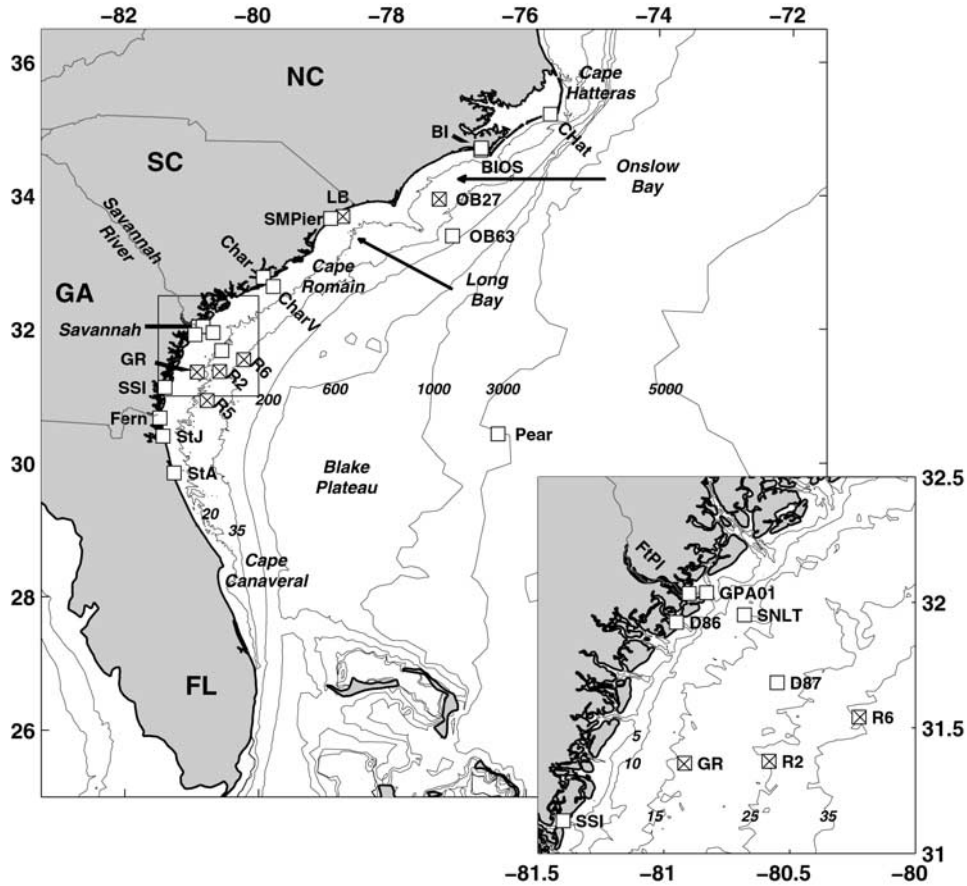

Figure 1. Study region. The South Atlantic Bight extends from Cape Hatteras, North Carolina, to Cape Canaveral, Florida. Water level stations are shown with squares. ADCP stations are shown with crosses. The 20, 35, 200, 600, 1000, 3000, and 5000-m isobaths are shown. The Bermuda water level station is not shown on this figure. The box is detailed in the inset. (inset) Close-up of the northern coast of Georgia. The 5, 10, 15, 25, and 35-m isobaths are shown.

the spatial locations of the water level gauges. A large portion of the ETIC must be included to properly model the M_2 tide. However, tidal dynamics in the SAB region, and the effects of the estuaries on the shelf-wide tidal characteristics, were not investigated in [*Lynch et al.*, 2004].

[5] The South Atlantic Bight region of the eastern United States coast extends from Cape Hatteras, North Carolina to Cape Canaveral, Florida (Figure 1). The continental shelf (shoreward of the 200-m isobath) is 10–30 km wide at the northern and southern extremes and broadens to 120 km off the Georgia coast. Bathymetric contours are parallel to the coast. The coast is perforated with a complex of estuaries and tidal inlets (henceforth, the estuary/tidal inlet complex, ETIC) from middle South Carolina to northern Florida. The Gulf Stream generally lies seaward of the 100-m isobath.

[6] The tidal environment in the SAB is a semidiurnal (primarily M_2) cooscillation with the North Atlantic deep ocean tide [*Redfield*, 1958]. Significant amplification occurs along the widest part of the continental shelf (off Georgia). The tidal velocity ellipse major axes are generally oriented cross-shelf, with minor axes lengths about half that of the major axis length [*Redfield*, 1958; *Clarke and Battisti*, 1981; *Werner et al.*, 1993]. The tidal Eulerian residual velocity is weak, with equatorward shelf break flow and poleward nearshore flow at about 0.01 m s^{-1} [*Werner et al.*, 1993]. Tidal contributions to the total water level and current variance are substantial. *Tebeau and Lee* [1979] and *Lee and Brooks* [1979] found that the variance in the tidal frequency band accounted for 80–90% and 20–40% of the cross-shelf and along-shelf current variance in the midshelf. Along with *Pietrafesa et al.* [1985], their results also demonstrated the cross-shelf nature of this variance partitioning: semidiurnal tides accounted for about 80% of inner and midshelf kinetic energy, while accounting for only about 30% of outer shelf energy.

[7] More specifically, *Redfield* [1958] considered the M_2 elevation and velocity along the Middle Atlantic Bight (MAB) and northern SAB from shelf stations. His analysis stopped at Savannah, Georgia, but indicated that the M_2 surface tide is a standing wave on the shelf in the MAB. This suggests that the large-scale coastal water level at semidiurnal frequencies is in phase along the coast and that maximum shoreward tidal velocities lead the time of high water by about one-quarter period. Redfield found that this was also true for the semidiurnal tide on the SAB shelf, at least as far south as Savannah: M_2 progresses slowly along the shelf break, and the time of maximum shoreward current leads the time of maximum water level by about 3 h. He

also demonstrated that the M_2 tide exhibited the largest cross-shelf amplification at the widest part of the continental shelf. The M_2 elevation at the shelf break of 0.5 m amplifies to about 1.0 m along the Georgia coast. He concluded that the semidiurnal tides along the U.S. east coast are a cooscillation with the open ocean North Atlantic tide, being forced at the shelf break. The character of the tide equatorward of Savannah was ambiguous.

[8] *Clarke and Battisti* [1981] and *Clarke* [1991] developed an analytical treatment describing cross-shelf tidal characteristics. They explained semidiurnal elevation amplification in midlatitude regions by constructive interference of inertia-gravity waves propagating cross-shelf. Diurnal tides, for which frequencies are near-inertial in the middle and lower SAB, cannot propagate shoreward as inertia-gravity waves, cannot constructively interfere, and hence do not amplify.

[9] *Chen et al.* [1999] examined inner shelf frontal mechanisms off the Georgia coast, including a contribution from tidal mixing. They provided solutions for the tides on a limited-area model domain that appear reasonable in amplitude and phase skill, despite the low resolution of the coastal zone and the neglect of the tidal inlet energy sinks. However, since the tides were included in this study to provide a background mixing environment, skill in tides was not rigorously assessed.

[10] *Lentz et al.* [2001] considered tidal observations in the lower MAB, from Cape Hatteras north toward the Chesapeake Bay entrance. Although geographically outside of the SAB, their results are of interest because they describe the mechanisms behind along-shelf variation in the semidiurnal tidal velocities. Using data analysis and a 2-D analytical model, along-shelf semidiurnal tidal variation is explained largely by increases in the shelf width from Cape Hatteras to the Chesapeake Bay entrance. The widening shelf induces a weak progressive wave component to the otherwise standing wave solution, which in turn develops a phase lag near the coast. Variations in diurnal tidal parameters were not sensitive to the primary mechanism in their analytical model (linearly increasing/decreasing shelf width) and are apparently not due to shelf width variations.

[11] Energy analyses for global ocean tides, derived from satellite altimetry and global tidal models [e.g., *Kantha et al.*, 1995], indicate that the bulk of energy input into the oceans occurs in the open ocean, due to lunar and solar gravitational loading. This input energy must eventually be dissipated, and a substantial portion is extracted by bottom friction in shallow marginal seas and on broad continental shelves (e.g., Yellow Sea [*Kang et al.*, 2002], northwest European shelf [*Davies and Kwong*, 2000], Patagonian shelf [*Glorioso and Flather*, 1997]). An additional portion of the input energy (as much as 30% [*Egbert and Ray*, 2000]) now appears to be shunted to the baroclinic tides in deep ocean regions like the Hawaiian Ridge and the Mid-Atlantic Ridge [*Kantha and Tierney*, 1997; *Ray and Mitchum*, 1997; *Munk*, 1997; *Egbert and Ray*, 2000; *Kang et al.*, 2000]. The tidal energy that is transported to the shelf from the deep oceans is dissipated through the retarding action of bottom friction that opposes the tidal motion on the shelf. Part of this dissipation occurs in nearshore regions where the tidal flow is enhanced by the presence of tidal inlets and estuaries, as in the SAB.

[12] While the total tidal dissipation on the SAB shelf is a small fraction of the global tidal power input ($\sim$1.8 GW versus $\sim$2.4 TW), and in fact a small fraction of the total dissipation in the North Atlantic Ocean ($\sim$0.7 TW), about 25% of the dissipation in the SAB occurs in the ETIC along the Georgia/South Carolina coast (see Results section). Basin or global scale tidal models typically do not (or cannot) include estuaries and tidal inlets, assuming that their effects are localized and do not affect the larger-scale solutions. We demonstrate that, while this assumption may be justified, the SAB local and regional tidal solutions at semidiurnal frequencies are fundamentally influenced by the ETIC. Since numerical model solutions of the SAB that are focused on shelf-scale performance (and some that are focused on inner shelf and nearshore processes) do not typically include nearshore geometries, it is difficult to accurately model the barotropic tides in the semidiurnal band with skill that compares to tidal modeling of other regions.

2. Data and Methods

[13] For this study, water level and velocity observations have been collected from a variety of sources in the SAB. Water level data sources include the following: bottom pressure records from several permanent midshelf deployments from the South Atlantic Bight Synoptic Offshore Observational Network (SABSOON [*Seim*, 2000]); temporary deployments in the region; and published water level harmonic constituents from NOS (Table 1 and Figure 1). These latter stations are generally located within the ETIC, which we broadly define as the wetted region landward of the sound limits. Bottom pressure records are converted to sea levels using the standard hydrostatic relationship. The published harmonic constituents from NOS stations are used assuming that they represent the most robust constituent estimates, given the long historical record from which the constituents are derived.

[14] Velocity data are comparatively less available and are limited to ADCP records from permanent deployments at two SABSOON tower locations and several short-term deployments: two in the SABSOON tower region and one each in Long Bay and Onslow Bay (Table 2 and Figure 1). The tidal current analysis is limited to the depth-averaged flow.

[15] Harmonic analysis of the water level and depth-averaged ADCP observations was performed using the MATLAB code *t_tide* [*Pawlowicz et al.*, 2002]. The time spans for the data are not contemporaneous. We have used the longest possible record length L at each station, which varies from 28 to 851 days. All data records were decimated to hourly values. We are primarily interested in M_2 and K_1. However, the Rayleigh frequency separation criterion $|\Delta f|L > 1$ between K_1 and P_1 requires a record length of 4192 h (about 175 d). Otherwise, the harmonic estimate of K_1 is contaminated with P_1 variance. P_1 can be inferred from K_1 if the ratio between the two can be estimated from records of sufficient duration. Using the water level and velocity harmonic analysis at the tower stations R2 and R6, the amplitude ratio $K_1/P_1 \sim 3$, and the phase difference $K_1 - P_1 \sim 0$. For records shorter than 175 d, we use this amplitude ratio and phase difference to infer P_1, and more

Table 1. Water Level Station Locations[a]

Station	Abbr	Longitude, °W	Latitude, °N	Depth, m	RL, days
Estuary					
Cape Hatteras, NC+	CHat	75.64	35.22	-	-
Beaufort Inlet, NC	BIOS	76.67	34.68	14.6	63
Beaufort Inlet, NC+	BI	76.67	34.72	-	-
Charleston, SC+	Char	79.93	32.78	-	-
Charleston Entrance, SC	CharV	79.78	32.64	14	28
Ft. Pulaski, GA+	FtPl	80.90	32.03	-	-
Georgia Port Auth.	GPA01	80.83	32.04	8.5	50
D86, Wassaw Sound, 1986	D86	80.95	31.92	4.5	45
St Simons Island, GA+	SSI	81.40	31.13	-	-
Fernandina Beach, FL+	Fern	81.47	30.67	-	-
St. Johns River, FL+	StJ	81.43	30.40	-	-
Shelf					
Onslow Bay 27, NC	OB27	77.30	33.95	35	250
Long Bay, NC	LB	78.74	33.69	14	39
Springmaid Pier, SC +	SMPier	78.92	33.66	-	-
Onslow Bay 63, NC	OB63	77.10	33.40	90	77
Sav'h Navigational Light Tower	SNLT	80.68	31.95	14	40
D87, FLEX 1987	D87	80.55	31.68	20	45
R6	R6	80.23	31.53	35	516
R2	R2	80.57	31.38	26	851
Gray's Reef, GA	GR	80.92	31.36	16	76
R5	R5	80.77	30.93	24	76
St. Augustine, FL+	StA	81.26	29.86	-	-
Deep					
Bermuda	Berm	64.42	32.22	-	365
Pearson	Pear	76.42	30.43	3766	180

[a]Stations marked with a superscript plus are NOS water level gauges. Abbr is the station abbreviation used in the text and figures. RL is the record length in days. Stations are grouped according to proximity to the ETIC of the Georgia/South Carolina coast. Estuary stations are generally located landward of the sound demarcation line (FtPl) or in the immediate vicinity of the coastal zone (e.g., D86). Shelf denotes stations that are offshore and removed from the immediate influence of tidal inlets/estuary mouths. This includes "beach" stations (e.g., StA) as well as midshelf stations (e.g., R2). Two Deep stations are included. Within each group, stations are listed from north to south. The source of the GPA01 observations is *Way* [1998]. The Bermuda station observations are from the Hawaii Sea Level Center, and the source of the Pearson station is *Pearson* [1975]. R2 and R6 are permanent SABSOON installations. GR and R5 are temporary SABSOON deployments.

appropriately determine K_1. This amplitude ratio and phase difference is consistent for other data locations in the SAB for which long records are available.

[16] Numerical solutions in the western North Atlantic Ocean are computed using ADCIRC-2DDI [*Luettich et al.*, 1992] which solves the vertically integrated, fully nonlinear shallow-water wave equations on linear triangular finite elements. This model is used in tidal simulations, storm surge calculations, and sediment transport studies, as well as in the operational oceanographic context [*Lynch et al.*, 2001; *Blanton*, 2003]. We use a standard quadratic bottom friction formulation with a drag coefficient of $C_d = 0.003$ and a minimum depth of 4.0 m. The model domain (Figure 2) extends westward from the only open boundary (60°W) and includes the Gulf of Mexico as well as a high-resolution representation of the ETIC along the coasts of Georgia, South Carolina, and North Carolina. Figure 2 also shows the nearshore detail and resolution in the vicinity of the Savannah River entrance. The model grid contains 63,076 nodes and 111,748 elements, with horizontal resolution ranging from 100 km in deep water, 2–10 km on the SAB shelf, to 50–100 m in the tidal inlets and estuaries. This latter resolution limits the model time step to 10 s. We refer to this domain as the "estuary" domain.

[17] The bathymetry is a combination of ETOPO5 in deep water, and NOAA's Coastal Relief Model on the SAB shelf and in the ETIC. Tidal amplitude and phase is specified along the open boundary, and the tidal potential is specified as well. The forcing spectrum is M_2, N_2, S_2, O_1 and K_1, extracted from the TOPEX-Poseidon altimeter-assimilated FES95.2 global tidal solutions [*Le Provost et al.*, 1998]. The model is integrated for 180 d, and harmonic analysis is performed at each model node over the second 90 d period of the integration.

[18] To investigate the impact of the ETIC on tides on the SAB shelf, an additional tidal solution is computed on a finite element domain that does not include the ETIC. All nodes landward of the sound limits have been removed, and the resulting new boundary segments are treated as no-normal-flow boundaries. This domain is otherwise the same as the above-described "estuary" grid and is referred to as the "no-estuary" grid (Figure 2, inset).

[19] Quantitative comparison between observed and modeled elevations is made by computing the complex error E between the values at each station:

$$E = \left| A_o e^{i\phi_o} - A_c e^{i\phi_c} \right|$$

where A_o, A_c and ϕ_o, ϕ_c are the observed and computed water level amplitudes and phases, respectively. Root-mean-square (rms) differences between observed and modeled values are used to quantify larger-scale error. For the estuary solution, all observation locations are within the model domain. For the no-estuary solution, several water level stations are outside of the domain. For these stations, the solution is sampled at the nearest grid location. Model solutions are shown primarily for the SAB region. Vector and ellipse plots are sampled onto a regular grid for visualization purposes. Elevation, velocity, orientation, and phase are reported in m, m s^{-1}, degrees (°), and Greenwich degrees (°G). Throughout the remainder of the paper, tables and figures report observations and model results from both model solutions, each discussed where appropriate.

3. Results

3.1. Observations

[20] The longest midshelf water level record (SABSOON tower R2, Table 3) shows that the main semidiurnal constituent is M_2, followed by N_2 and S_2. The largest diurnal

Table 2. Velocity Station Locations From Which ADCP Records Are Available[a]

Station	Abbr	Longitude, °W	Latitude, °N	Depth, m	RL, days
Onslow Bay 27	OB27	77.30	33.95	35	671
Long Bay, NC	LB	78.74	33.69	14	39
R6	R6	80.23	31.53	35	913
R2	R2	80.57	31.38	26	547
Gray's Reef, GA	GR	80.92	31.36	16	76
R5	R5	80.77	30.93	24	76

[a]Abbr is the station abbreviation used in the text and figures. RL is the record length in days. R2 and R6 are permanent SABSOON installations. GR and R5 are temporary SABSOON deployments.

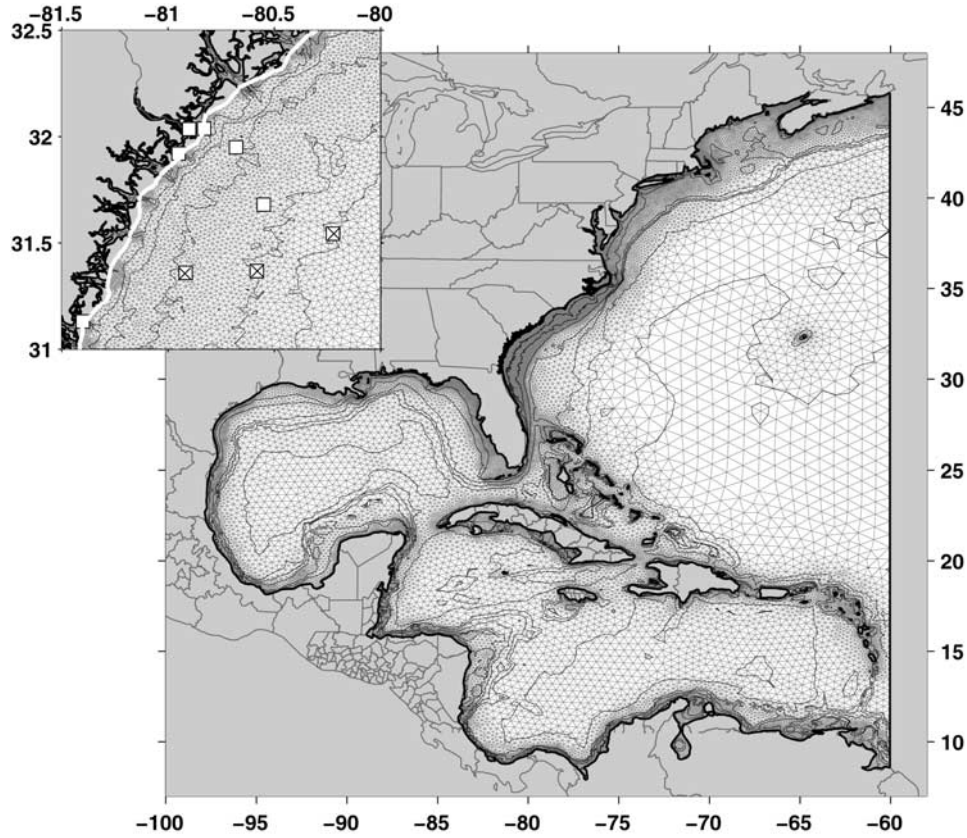

Figure 2. ADCIRC finite element model domain used for tidal computations in the northwest North Atlantic Ocean. The mesh contains 63,076 nodes, 111,748 elements. The 20, 35, 200, 600, 1000, 3000, and 5000-m isobaths are shown. The inset shows the grid detail in the region off of the northern coast of Georgia. The thick white line is a typical landward boundary for model domains that do not include the ETIC along the Georgia/South Carolina coast. The 5, 10, 15, 25, and 35-m isobaths are shown. The white squares mark the same stations as in the inset of Figure 1.

tides are K_1 and O_1. The published harmonic constituents for the NOS stations show that the same semidiurnal and diurnal frequencies dominate the coastal station tides. This is typical of other U.S. east coast regions and has been reported by others, including *Moody et al.* [1984]. The annual and semiannual steric anomaly tides (S_A and S_{SA}) are not small (0.14 m and 0.08 m, respectively). M_2 and K_1 account for about 92% and 57% of the total semidiurnal and diurnal variance, respectively.

[21] Table 4 reports the observed water level amplitude and phase for the constituents M_2, N_2, S_2, K_1 and O_1, and includes published values for NOS stations. Observed M_2 water level amplitudes are largest in the Savannah, Georgia, region (e.g., FtPl, GPA01) at about 1.0 m. Amplitudes decrease to the north and south, to 0.66 m at St. Augustine and 0.45 m at Cape Hatteras, respectively. Although there are no directly cross-shelf station sequences, the Onslow Bay stations (OB63 and OB27) in the northern part of the region show typical semidiurnal cross-shelf amplification: from 0.46 m closer to the shelf break (OB63) to 0.55 m at about midshelf (OB27). This is also seen at the SABSOON tower region, where the amplitude increases from 0.68 m at the R6 tower to 0.89 m at the GR station.

[22] The general equatorward phase propagation of all constituents is noted. In the cross-shelf direction, all constituents are largely in phase in the northern part of the SAB (OB63, OB27). In the middle SAB region, the M_2 phase increases shoreward, from 3.0° at R6 to 10° at the GR station (the latest midshelf value). The latest phases occur at

Table 3. Fifteen Largest Tidal Constituents From the Harmonic Analysis of the SABSOON R2 Water Level Record[a]

Constit	A	ϕ	SNR
M_2	0.76	7.2	20000
N_2	0.18	345.2	1000
S_A	0.14	252.6	80
S_2	0.13	29.0	560
K_1	0.10	193.6	4700
S_{SA}	0.08	44.5	26
O_1	0.08	199.7	2400
H_1	0.04	230.6	51
ν_2	0.04	348.5	46
H_2	0.03	135.0	43
P_1	0.03	193.5	510
K_2	0.03	37.1	33
M_{SM}	0.03	15.0	2
$2N_2$	0.02	325.8	18
T_2	0.02	39.1	17

[a]The record is 851 days long. The tidal analysis explains 95.9% of the total water level variance. The given constituents contain 99.2% of the total tidal variance. The record is long enough that all frequencies are ranked as significant. "SNR" is the signal-to-noise ratio estimate from the analysis.

Table 4. Observed Tidal Water Level Amplitudes (m) and Phase (°G) for Elevation Stations Listed in Table 1[a]

	M_2		N_2		S_2		K_1		O_1	
Station	A	ϕ	A	ϕ	A	ϕ	A	ϕ	A	ϕ
					Estuary					
CHat+	0.45	353.2	0.11	331.3	0.08	16.2	0.09	184.6	0.08	186.4
BIOS	0.55	352.1	0.15	335.1	0.10	25.1	0.10	199.7	0.07	195.3
BI+	0.44	7.3	0.10	349.7	0.07	31.8	0.08	198.5	0.06	204.7
Char+	0.76	12.3	0.18	353.7	0.12	36.5	0.11	198.0	0.08	204.9
CharV	0.71	357.4	0.19	346.7	0.09	36.3	0.10	190.1	0.07	196.1
FtPl+	1.03	17.9	0.23	2.1	0.16	48.4	0.11	201.0	0.08	207.3
GPA01	0.95	9.5	0.26	351.5	0.16	41.2	0.13	210.9	0.08	196.5
D86*	0.96	16.8	0.21	15.1	0.22	35.3	0.11	207.6	0.07	203.4
SSI+	0.97	23.8	0.21	6.1	0.15	50.8	0.11	201.3	0.08	206.4
Fern+	0.90	32.9	0.20	14.7	0.14	61.2	0.11	208.0	0.08	215.9
StJ+	0.67	26.0	0.16	5.8	0.10	50.0	0.08	203.3	0.06	211.4
					Shelf					
OB27	0.55	353.3	0.14	335.8	0.10	17.0	0.09	184.1	0.07	189.3
LB	0.73	358.6	0.15	344.0	0.12	15.0	0.12	186.8	0.07	199.5
SMPier+	0.75	357.7	0.17	337.9	0.13	18.8	0.10	189.3	0.08	193.3
OB63*	0.46	352.6	0.12	320.4	0.07	27.6	0.09	201.1	0.07	188.4
D87*	0.83	4.9	0.16	341.1	0.18	13.0	0.10	193.3	0.07	196.7
SNLT*	0.89	6.3	0.20	2.4	0.20	19.3	0.10	195.3	0.07	194.9
R6	0.68	1.5	0.17	339.7	0.13	28.0	0.10	190.9	0.07	198.0
R2	0.76	7.2	0.18	345.2	0.13	29.0	0.10	193.6	0.08	199.7
GR*	0.88	9.5	0.19	344.9	0.15	29.1	0.11	189.2	0.07	199.4
R5*	0.76	8.0	0.17	341.7	0.13	26.8	0.11	190.2	0.07	196.3
StA+	0.66	14.3	0.16	354.8	0.11	35.7	0.10	197.0	0.07	202.4
					Deep					
Berm	0.35	358.7	0.08	340.1	0.08	26.9	0.07	186.0	0.05	191.3
Pear	0.45	357.6	0.11	335.7	0.08	23.1	0.10	190.0	0.07	194.3

[a]Stations marked with a superscript plus are NOS water level gauges, and stations marked with a superscript asterisk have P_1 infered from K_1. The 95% confidence intervals are as follows (except for NOS stations): Amplitude errors are less than 0.03 m. M_2 phase intervals are 2° for CharV and GPA01, and less than 1° elsewhere. N_2 intervals are 4°–8° for short records, and 1°–2° for longer records. S_2 intervals range from 1°–8°, except for CharV where it is 18°. K_1 intervals range from 1°–3°. O_1 intervals range from 1°–7°.

the coastal stations that are well within the sound limits (e.g., SSI, FtPl). K_1 and O_1 tides show comparatively little along-shelf variation in water level amplitudes, 0.09 m to 0.11 m and 0.07 m to 0.08 m, respectively. Cross-shelf amplification is minimal.

[23] Tidal ellipse parameters (semimajor/semiminor axes, orientation, and Greenwich phase) from the velocity observations are given in Table 5 for the major tidal constituents from the SABSOON tower R6. The largest component is M_2, with a cross-shelf velocity of 0.29 m s^{-1}. All constituents rotate clockwise (the semiminor axes are all less than zero). For both the M_2 and K_1 frequencies, tidal ellipses are oriented perpendicular to the isobaths with ellipse eccentricities (major/minor axis length) approximately ω/f, where f is the Coriolis parameter and ω is the tidal frequency. For semidiurnal tides, this ratio is 1.8 (at 32°N) and the eccentricity is about 2.7. For diurnal tides, ω is closer to f at midshelf latitudes, and the eccentricity is closer to 1.0.

[24] M_2 and K_1 tidal ellipse parameters for all stations are reported in Table 6 and Figure 3. M_2 major axis lengths in the SABSOON region are 0.30 m s^{-1} in the midshelf (R2, R6) and decrease shoreward to 0.25 m s^{-1} (GR). In the nearshore region (LB), the ellipse becomes more rectilinear. The phase ranges from 261° to 290°, and ellipse inclinations are oriented cross-shelf. K_1 velocities are an order of magnitude smaller than M_2 and also oriented cross-shelf. The phase ranges from 100° to 135°, except at the short-record stations GR and R5. We note that at the LB station, the tidal ellipse rotates counterclockwise for both frequencies.

[25] An interesting component to the water level analysis is the annual variation in the harmonic constituents. Figure 4 shows amplitude and phase for M_2 at Fort Pulaski, Georgia, computed from 10 years of NOS water level data. The harmonic analysis is performed on 31-day segments and averaged over each month. The mean M_2 amplitude is about 1.0 m ± 0.025 m and the mean phase is 18° ± 4°. The amplitude variance about each month is about 0.013 m, and 2° in phase. Variation is expected in the tidal current harmonics where seasonal stratification affects the vertical profile of the horizontal current [e.g., *Mofjeld*, 1976; *Prandle*, 1982]. It has also been seen in water level harmonics by *Kang et al.* [1995] (Yellow Sea), *Foreman et al.* [1995] (Victoria Sound), and *Ray and Mitchum* [1997] (Hawaiian Ridge). This is usually attributed to seasonal stratification, which diverts barotropic tidal energy into the baroclinic tide [*Kang et al.*, 2002; *Ray and Mitchum*, 1997]. The same level of variability is seen in the analysis of the midshelf SABSOON tower pressure records, but the series are not yet long enough for robust error estimates. We are not aware of strong evidence of internal tides in the SAB. However, *Ryan and Yoder* [1996] hypothesize that observed pigment concentrations in the SAB, which were maximum along the shelf break, could be a result of internal tides that have been observed in coastal SAB waters [*Shanks*, 1988]. There is also recent evidence from satellite altimetry analysis of internal tides seaward of the shelf break of the SAB [*Kantha and Tierney*, 1997; *Carrère et al.*, 2004]. The extent to which these internal tides generated at the shelf break might affect coastal tides is not clear.

[26] In the remaining sections of the paper, we will focus on the main semidiurnal (M_2) and diurnal (K_1) tidal constituents in terms of characteristics of the observations and model solutions. These components represent the bulk of the tidal frequency variance in the SAB, and they have the largest signal-to-noise ratio in their respective tidal species groups. The characteristics of the other constituents that are

Table 5. Harmonic Analysis of the SABSOON Tower R6 Depth Averaged Velocity Over the 913-Day Period Starting 1 April 2000[a]

Constit	Semimajor	Semiminor	Inclination	Phase	SNR
M_2	0.289	−0.105	149.2	278.5	51000
N_2	0.068	−0.025	149.5	258.6	2800
S_2	0.051	−0.019	150.7	301.4	1600
K_1	0.019	−0.011	136.9	107.3	350
O_1	0.013	−0.011	119.2	125.8	180
L_2	0.014	−0.004	155.3	292.0	120
ν_2	0.013	−0.005	147.5	254.7	100
P_1	0.007	−0.002	148.5	97.0	46

[a]Axes lengths are in m s^{-1}, inclination is in degrees CCW from east, and the phase is in degrees GMT. Sixty-eight tidal constituents were separable in the data record, which accounts for 89% and 67% of the east/west and north/south velocity components, respectively. The major (minor) tidal ellipse axes listed account for 97% (99%) of the total tidal major (minor) axis variance. The 95% confidence intervals are ±0.001 m s^{-1} for all axis lengths and (0.3, 1.3, 1.7, 5.5, 15.8, 5.5, 7.2, 9.5) degrees for inclination and phase, in the order listed above.

Table 6. M_2 and K_1 Ellipse Parameters From Depth-Averaged ADCP Observations and Model Solutions Sampled at Observation Locations[a]

	Semimajor Axis			Semiminor Axis			Inclination			Phase		
Station	Obs	Est	NoEst	Obs	Est	NoEst	Obs	Est	NoEst	Obs	Est	NoEst
						M_2						
OB27	0.116	0.139	0.131	−0.058	−0.068	−0.062	119.0	139.4	137.9	261.4	255.7	261.0
LB	0.071	0.071	0.064	0.014	0.012	−0.003	138.2	139.7	144.9	272.6	267.7	269.4
R6	0.289	0.308	0.258	−0.105	−0.107	−0.092	149.2	154.3	156.4	278.5	275.7	267.5
R2	0.312	0.330	0.271	−0.105	−0.103	−0.084	146.5	152.1	155.1	287.0	283.6	273.6
GR	0.249	0.282	0.218	−0.067	−0.059	−0.037	148.5	155.3	160.6	285.6	285.0	273.7
R5	0.297	0.321	0.271	−0.092	−0.103	−0.086	144.5	151.0	153.7	289.6	287.9	278.3
Rms		0.022	0.028		0.007	0.018		9.7	11.2		3.6	9.8
						K_1						
OB27	0.011	0.013	0.013	−0.007	−0.008	−0.008	70.7	104.0	102.7	132.3	108.4	114.5
LB	0.009	0.005	0.005	0.003	0.002	0.001	162.4	132.8	153.5	124.0	101.1	106.0
R6	0.019	0.021	0.019	−0.011	−0.012	−0.012	136.9	134.7	136.9	107.3	110.5	107.1
R2	0.022	0.024	0.020	−0.010	−0.011	−0.010	121.5	132.1	134.7	115.8	118.7	114.8
GR	0.020	0.018	0.015	−0.013	−0.006	−0.005	26.0	140.4	146.2	235.8	112.0	104.8
R5	0.012	0.023	0.021	−0.004	−0.011	−0.011	175.1	133.4	135.8	96.4	121.3	117.2
Rms	-	0.003	0.002	-	0.001	0.001	-	22.9	17.9	-	16.8	12.7

[a]Axes lengths are in m s^{-1}, inclination is in degrees CCW from east, and phase is in °G. The "estuary" ("no-estuary") solution is given in the Est (NoEst) column. The Rms rows are the root-mean-square differences in the tidal parameters between the observations and the two model solutions. Axis length errors (in the order listed above) are ±0.001 m s^{-1} for long records, and ±0.003 – 0.007 m s^{-1} for shorter records (R5, GR). Phase and inclination errors for M_2 are 0.8°, 1.6°, 0.3°, 0.9°, 1.6°, 1.5°. K_1 errors are comparatively larger: 20°, 20°, 6°, 12°, 50°, 50°. The K_1 rms statistics do not include the GR and R5 stations.

close in frequency to M_2 and K_1 are qualitatively similar but with reduced magnitudes.

3.2. Tidal Model Solution With ETIC

[27] The harmonic analysis of the model integration is shown in Figure 5 for M_2 and K_1. The M_2 amplitude (Figure 5, top) shows strong amplification on the SAB shelf, focused in front of the ETIC. Coamplitude lines are generally parallel to each other, and range from about 0.5 m at the shelf break to 1.0 m immediately in front of the ETIC. Little amplification occurs at the northern and southern extreme ends of the SAB. Cophase lines progress equatorward along the shelf break and show a distinct onshelf turning at the shelf break. The greatest phase lag at the coast, relative to that of the shelf break, occurs near the Florida/Georgia border. The cross-shelf phase difference ranges from about 0° at the northern end of the SAB to 18° in the middle SAB.

[28] For the K_1 constituent, the cross-shelf amplification is weak. The phase progresses equatorward, also with onshelf turning at the shelf break, but without as large of a cross-shelf phase lag seen in M_2. We note that the large-scale character of the K_1 tide is consistent with equatorward propagation as a Kelvin-like wave.

[29] The model tidal velocities (Figure 5, bottom) for M_2 show a substantial increase in energy shoreward of the shelf break, with maxima in the central midshelf region. Cross-

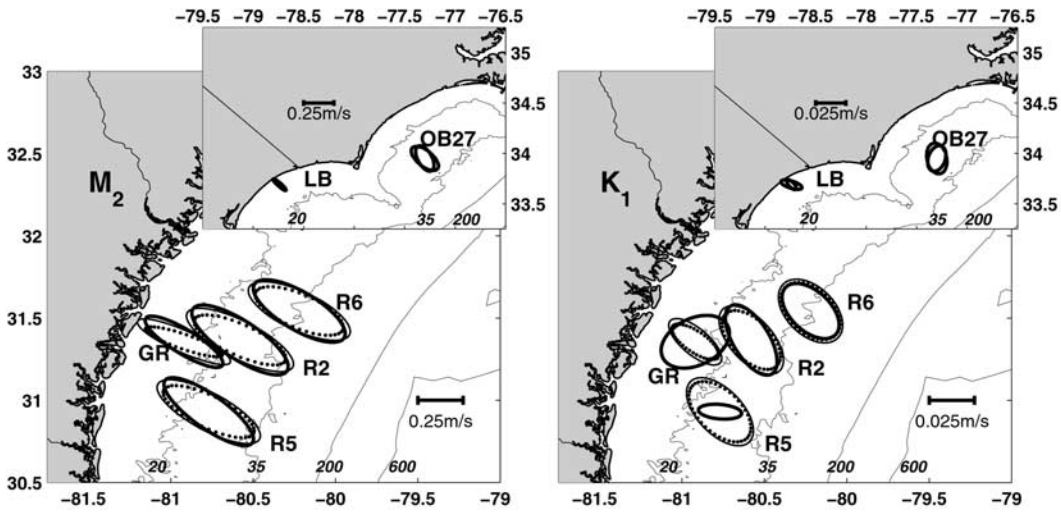

Figure 3. Observed versus computed (with and without estuaries) M_2 and K_1 tidal ellipses for the depth-averaged velocity at the ADCP stations. The inset shows the Onslow Bay and Long Bay ellipses. Thick/solid ellipses are observations, thin/solid ellipses are from the "estuary" solution, and dotted ellipses are from the "no-estuary" solution. The 20, 35, 200, and 600-m isobaths are shown.

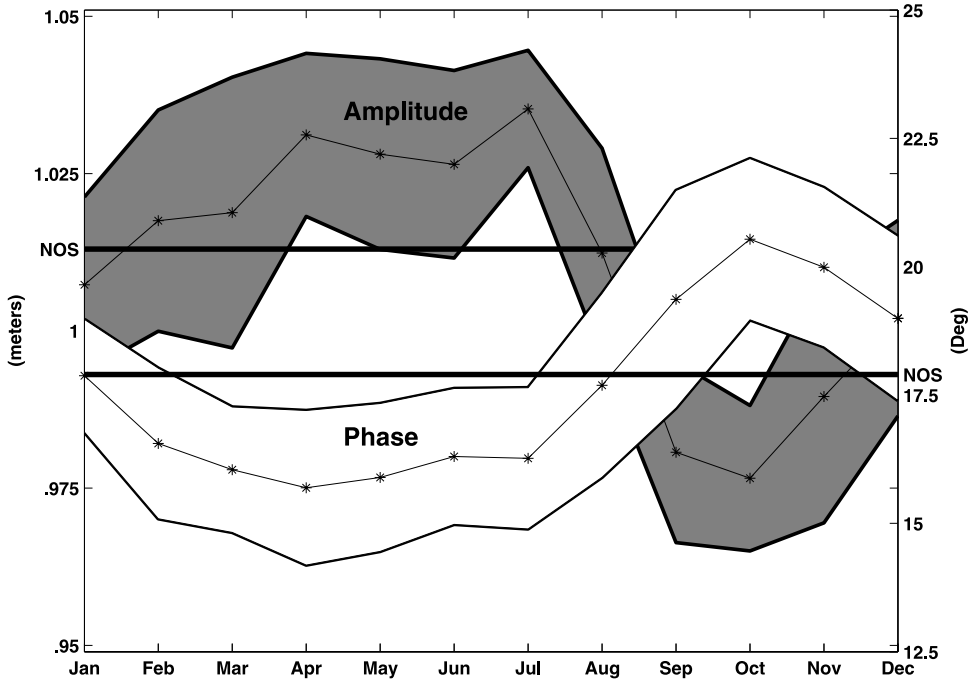

Figure 4. Annual variation in the M_2 amplitude (gray) and phase (white) at the NOS Fort Pulaski, Georgia, water level station. The harmonic analysis is done in 31-day segments, over 10 years of water level data, and averaged over each month. Monthly means are plotted with symbols and the 95% confidence intervals are included. The NOS published values for amplitude (1.013 m) and phase (17.9°) are shown with the solid lines. The data shown are the same as in Figure 3 in *Lynch et al.* [2004].

shelf amplitudes reach 0.30 m s^{-1} at the widest part of the shelf, and the phase indications (direction of flow at t = 0) are directed along-shelf poleward. K_1 tidal velocities are 10% of the M_2 velocities, with midshelf maxima as well. Note that the K_1 ellipse eccentricity is generally more circular compared to M_2. The phase indicator (flow direction at t = 0) is directed along-shelf equatorward. For K_1, the velocity phase exhibits more spatial structure than that of M_2. For both frequencies, the tidal velocities rotate clockwise except very near the coast where the rotation direction is variable and over the southern portion of the Blake Plateau.

3.3. Tidal Model Solution Without ETIC

[30] The M_2 model solution without the ETIC (''no-estuary'') shows fundamental differences with the ''estuary'' solution and a degradation in the agreement with the observations (see section 3.4) for both tidal velocity and elevation, as given in Tables 6 and 7. This solution has substantial phase leads and reduced elevation in the nearshore region, with the complex error ranging 0.05 m to 0.54 m. The midshelf stations D87, SNLT, R6, R2, GR and R5, which are seaward of the ETIC, also show increased error that results mostly from a phase lead. For the shelf stations away from the ETIC (OB27, OB63, LB), there is only a small increase in the elevation error. For the tidal ellipse parameters, the rms error is doubled (from 0.01 m s^{-1} to 0.02 m s^{-1}), and the phase error is larger by a factor of 3.

[31] In Figure 6, the M_2 and K_1 amplitude ratios (estuary divided by no-estuary) and phase differences (estuary minus no-estuary) are shown for the middle SAB. The amplitude ratio for M_2 ranges from 1.0 (no amplification) to about 1.1 (a 10% increase in elevation) at the coast, and the phase is lagged by 1° to 9°. The K_1 tide does not show such differences in elevation between the two solutions; there is no amplification, and only a small 1° to 3° phase lag from about midshelf shoreward.

[32] The presence of the estuaries increases the tidal velocities in M_2, particularly in the major axis, which is directed shoreward. The differences in the two model solutions are quantified in Table 6, which reports the tidal ellipse parameters for M_2 and K_1 at the ADCP locations for the observations and model solutions. The M_2 phase is later in the estuary solution. Tidal velocity amplification is concentrated in the region of the ETIC and extends past the midshelf. K_1 shows a small increase in the major axis length but little change in the minor axis length or phase. The rms error of the axis lengths and phases for M_2 is substantially reduced in the estuary solution, as compared to the no-estuary solution.

[33] The K_1 error (E in Table 7) is not as affected as M_2 by removing the estuaries. For K_1, the amplitude is modeled well in both solutions, but the no-estuary solution exhibits some large phase leads at the estuary stations. The complex error increases for the estuary stations due more to a phase lead rather than to underpredicting the elevation. The shelf stations are not significantly affected, nor are the two deep stations. The rms statistic for K_1 does not include stations R5 and GR since the ellipse parameters are suspect.

3.4. Observations Versus Model Solutions

[34] Comparison of the model solutions (with and without inclusion of the ETIC) to the observed M_2 and K_1 water levels is given in Table 7. The M_2 complex error E for the

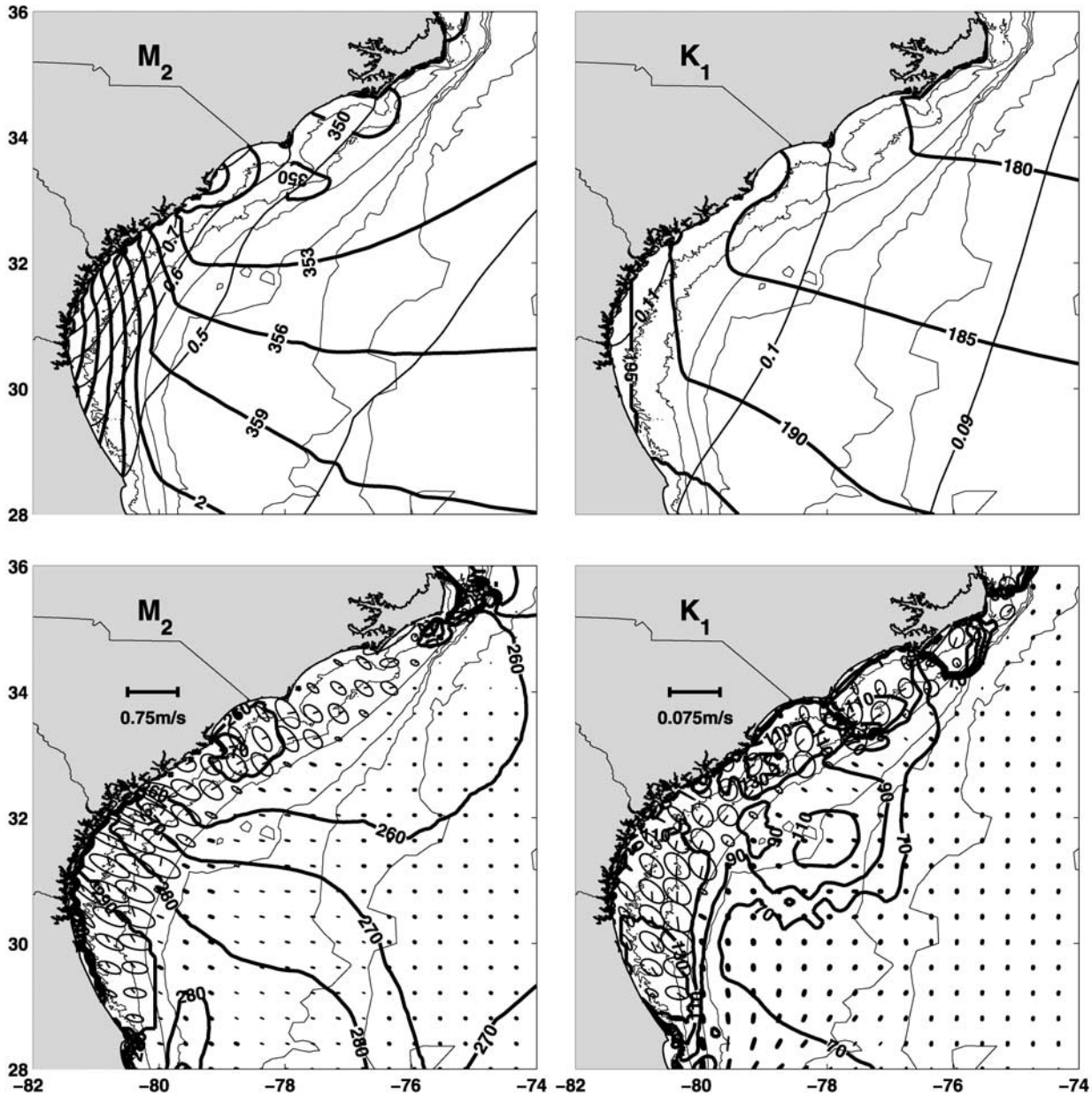

Figure 5. (top) Computed (with ETIC) M_2 and K_1 elevation. Thin black lines are amplitude (m). Thick black lines are phase (°G). For the M_2 elevation amplitude and phase, the contour interval is 0.1 m and 3°. (bottom) Computed (with ETIC) M_2 and K_1 tidal ellipses. All ellipses rotate clockwise, except very near the coast and in the southwest area of the Blake Plateau. Thick black contours are the Greenwich phase, in degrees. The ticks originating at the ellipse centers are the direction of flow at t = 0 h, GMT. The 20, 35, 200, 600, 1000, 3000, and 5000-m isobaths are shown with the thin grey lines.

deep station Pear is 0.04 m (0.05 m) for the estuary (no-estuary) solution. The comparison to the no-estuary solution is as follows: the complex error ranges from 0.03 m to 0.26 m for the shelf stations, and from 0.05 m to 0.49 m for estuary stations. The estuary solution exhibits significant improvement over the no-estuary solution. For the estuary and shelf stations, E ranges from 0.01 m to 0.15 m and 0.01 m to 0.06 m, respectively. The M_2 phase is underpredicted by the no-estuary solution, particularly for the estuary stations. The amplitude and phase are shown separately in Figure 7. The complex error in the estuary solution at station BI is 0.15 m. This large error is due to the bathymetry in the region which is not resolved well enough. Higher resolution model solutions of the North Carolina coast show better skill in the ETIC in this region [*Luettich et al.*, 1999].

[35] Tidal ellipse parameters for M_2 (Table 6) show good agreement between the observations and the estuary solution. There is improvement in the rms skill measure over the no-estuary solution, particularly in phase (from 9.8° to 3.6°) and the minor axis lengths (from 0.017 m s^{-1} to 0.007 m s^{-1}).

Table 7. Modeled M_2 and K_1 Water Level Amplitude (m), Phase (°G), and Complex Error E (m) at the Water Level Stations

	M_2						K_1					
	Est			NoEst			Est			NoEst		
Station	A	ϕ	E	A	ϕ	E	A	ϕ	E	A	ϕ	E
						Estuary						
CHat	0.43	351.6	0.02	0.25	350.6	0.20	0.09	178.6	0.01	0.07	175.8	0.02
BIOS	0.54	349.6	0.03	0.52	347.3	0.05	0.10	180.6	0.03	0.10	179.6	0.03
BI	0.55	355.1	0.15	0.52	347.3	0.19	0.10	183.8	0.03	0.10	179.6	0.03
Char	0.76	4.6	0.10	0.49	351.4	0.35	0.11	191.8	0.01	0.09	181.9	0.04
CharV	0.71	353.4	0.05	0.66	351.5	0.09	0.10	186.2	0.01	0.10	185.4	0.01
FtPl	0.97	16.6	0.07	0.85	358.1	0.37	0.11	198.3	0.01	0.11	189.6	0.02
GPA01	0.96	9.9	0.01	0.85	358.1	0.20	0.11	194.6	0.04	0.11	189.6	0.05
D86	0.98	11.2	0.10	0.53	358.7	0.49	0.11	195.4	0.02	0.08	184.7	0.04
D87	0.83	3.8	0.02	0.77	358.6	0.11	0.11	190.7	0.01	0.11	189.4	0.01
SSI	0.98	23.8	0.01	0.64	8.6	0.39	0.11	201.4	0.00	0.09	191.0	0.03
Fern	0.89	36.9	0.06	0.41	11.0	0.54	0.11	207.9	0.00	0.08	187.9	0.04
StJ	0.59	23.9	0.08	0.54	10.4	0.21	0.09	207.0	0.01	0.09	191.4	0.02
						Shelf						
OB27	0.53	350.6	0.03	0.52	351.1	0.03	0.10	181.8	0.01	0.10	181.8	0.01
LB	0.70	354.4	0.06	0.67	354.8	0.07	0.10	185.2	0.02	0.10	184.7	0.02
SMPier	0.71	355.3	0.05	0.42	357.2	0.33	0.10	185.7	0.01	0.08	180.7	0.02
OB63	0.44	350.2	0.02	0.44	350.2	0.03	0.10	180.7	0.01	0.10	180.7	0.01
SNLT	0.91	4.8	0.03	0.83	358.0	0.14	0.11	191.6	0.01	0.11	189.4	0.01
R6	0.70	0.2	0.03	0.66	356.8	0.06	0.11	188.4	0.01	0.11	187.9	0.01
R2	0.78	5.0	0.04	0.74	0.3	0.09	0.11	191.1	0.01	0.11	190.0	0.01
GR	0.88	9.6	0.00	0.83	3.1	0.11	0.11	193.9	0.01	0.11	192.0	0.01
R5	0.76	8.1	0.00	0.74	3.3	0.07	0.11	192.6	0.01	0.11	191.7	0.00
StA	0.67	12.4	0.02	0.40	10.1	0.26	0.11	195.8	0.01	0.08	190.1	0.02
						Deep						
Berm	0.34	354.1	0.03	0.34	354.0	0.03	0.06	178.6	0.01	0.06	178.6	0.01
Pear	0.41	356.2	0.04	0.40	355.8	0.05	0.09	186.1	0.01	0.09	186.0	0.01

[36] For the K_1 tide, E ranges from 0.00 m to 0.04 m for all stations. Tidal ellipse parameter comparisons are given in Table 6 and Figure 3. Although the K_1 tidal current speeds are represented well in the model solution, there is some discrepancy with the inclination and phase for the stations with shorter record lengths (R5, GR). However, at the SABSOON towers R2 and R6, the phases are within 10° of the observations.

3.5. Impact of the ETIC on Tidal Solutions in the SAB

[37] The effects of including the ETIC in the SAB are summarized for M_2 in Table 8 and Figure 7, in which the

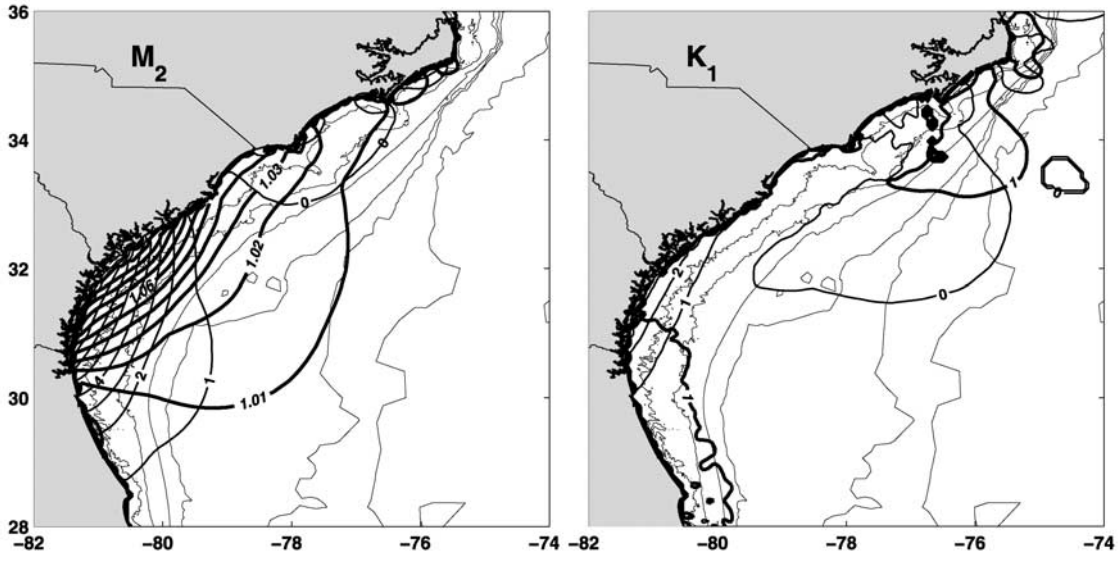

Figure 6. M_2 and K_1 amplitude ratio (estuary divided by no-estuary) and phase difference (estuary minus no-estuary) in the SAB from tidal model solutions with and without inclusion of the ETIC. Thick lines (and italics labels) are the amplitude ratio, and thin lines are the phase difference. The bathymetry is shown with the grey lines (20, 35, 200, 600, 1000, 3000, and 5000-m isobaths).

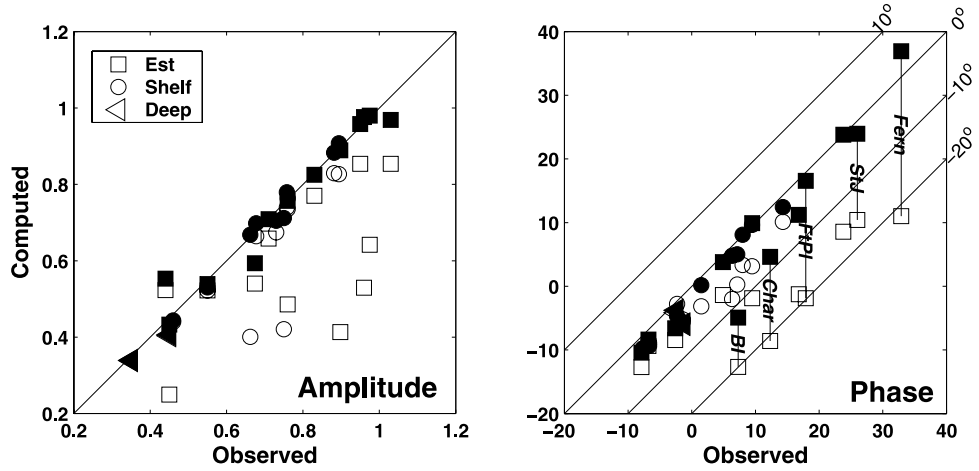

Figure 7. Observed versus computed M_2 amplitude (m) and phase (°G). Open symbols represent the "no-estuary" solution; solid symbols are with inclusion of the ETIC ("estuary"). The stations are grouped into Deep (triangle), Shelf (circle), and Estuary (square). The 1:1 line is plotted, as well as the 10°, −10°, and −20° error lines for the phase. The phase change for several stations is marked by the vertical lines and station labels.

elevation stations are grouped by deep, shelf and estuary stations, according to Table 1. The table gives the rms complex errors between the observations and the both model solutions. (The estuary rms values do not include the station BI for the reasons mentioned above.) The reduction in elevation and phase error is evident, with the deep water stations experiencing little change. Estuary amplitude errors are decreased from 0.25 m to 0.03 m, and the phase errors are reduced from 13.8° to 2.8°. Shelf station errors are reduced seven- and two-fold for amplitude and phase, respectively. Table 8 also includes the K_1 rms statistics. We note that this frequency is not as impacted by the resolution of the ETIC, given the confidence intervals on the diurnal constituents. Figure 7 shows the observed and computed M_2 elevation amplitude and phase. The improvement in phase for several stations is indicated by connecting lines and labels.

3.6. Tidal Energetics in the SAB

[38] We examine the nature of the tidal characteristics on the SAB shelf and in the adjacent deep ocean through diagnosis of the tidal energetics at the M_2 and K_1 frequencies. Generally, waves in the open ocean (removed from reflective/dissipative boundaries) are largely progressive and transport the tidal energy input in deep ocean regions to shallow regions where it is dissipated through bottom friction. Along the way, some energy is transfered to the baroclinic tide through the interaction of the surface tide with underlying topographic features in the presence of stratification [*Kantha and Tierney*, 1997; *Ray and Mitchum*, 1997; *Munk*, 1997; *Egbert and Ray*, 2000; *Kang et al.*, 2000].

[39] In its most basic form, the local tidal energy balance can be written as [*Egbert and Ray*, 2000]:

$$W - \epsilon = \nabla \cdot \mathbf{F} \tag{1}$$

where W is the local work rate, ϵ is the dissipation rate, and the right-hand side is the divergence of the energy flux $\mathbf{F}$ (equation (2)). Except in the deep ocean, where the bulk of tidal energy is input into the global oceans [*Kantha*, 1995], the work term is negligible and the dissipation rate is largely balanced by the flux divergence term.

[40] The energy "path" is indicated by the net energy flux vector $\mathbf{F} = (F_x, F_y)$ over a tidal period. We diagnose this flux from the tidal model solutions according to [*Pugh*, 1987]:

$$F_x = \frac{1}{2}\rho g h \eta U \cos\left(\phi_\eta - \phi_U\right)$$
$$F_y = \frac{1}{2}\rho g h \eta V \cos\left(\phi_\eta - \phi_V\right) \tag{2}$$

where $h(x, y)$ is the undisturbed water column depth, (η, ϕ_η) are the amplitude and phase of the computed water level, (U, ϕ_U) and (V, ϕ_V) are the amplitude and phase of the computed east and north velocity components, respectively. ρ is a reference density (1024 kg m^{-3}) and g is gravity. The term $\cos(\phi_\eta - \phi_{U,V})$ is the phase angle between the water level and depth-averaged velocity.

Table 8. M_2 and K_1 rms Differences Between the Water Level Observations and the Model Solutions, With and Without Inclusion of the ETIC[a]

	A		ϕ		E	
	NoEst	Est	NoEst	Est	NoEst	Est
			M_2			
Deep	0.03	0.03	3.5	3.4	0.04	0.04
Shelf	0.14	0.02	4.9	2.2	0.15	0.03
Estuary	0.25	0.03	13.8	2.8	0.31	0.05
			K_1			
Deep	0.01	0.01	5.9	5.9	0.01	0.01
Shelf	0.01	0.01	4.7	3.2	0.01	0.01
Estuary	0.02	0.01	15.1	9.3	0.03	0.02

[a]The complex error (E) and amplitude (A) are in meters, and the phase (ϕ) is in degrees GMT. The rows are organized as Estuary, Shelf, and Deep as in Table 1. The rms statistics do not include the stations BI and BI-OS.

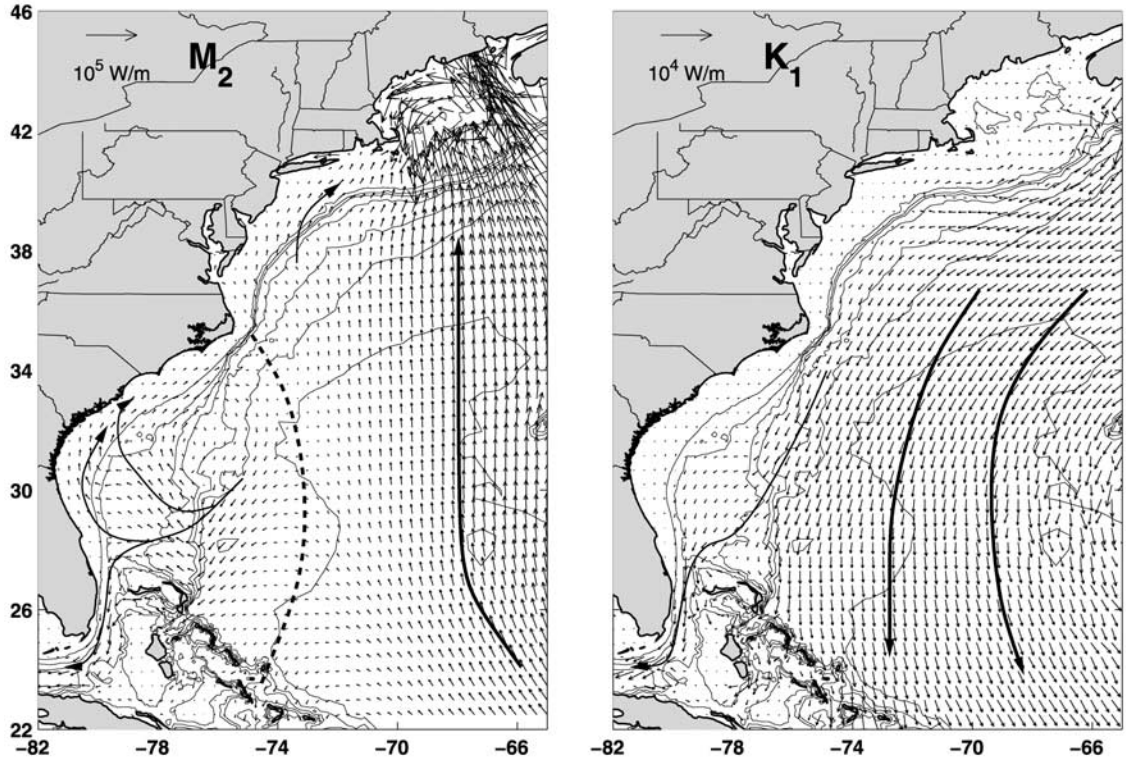

Figure 8. M_2 and K_1 energy flux in the SAB, diagnosed from the elevation and velocity solutions that include the ETIC in the SAB. Note that the vector scaling is different between the frequencies. Large arrows sketch the energy paths discussed in the text. The 200, 600, 1000, 2000, 3000, 4000, and 5000-m isobaths are shown.

[41] Figure 8 shows the energy flux for M_2 and K_1 for most of the model domain. For M_2, energy is transported poleward in the deep ocean toward the Gulf of Maine, a region known for large tidal velocity and elevation. Semidiurnal tidal energy enters the SAB by flowing equatorward along the eastern edge of, and then westward across, the Blake Plateau. Some of this energy continues equatorward through the Florida Straits and into the Gulf of Mexico. The remainder progresses shoreward onto the southern portion of the SAB. A weaker poleward energy flux occurs along the entire continental shelf, which is minimal where the shelf is most narrow and is largest where the shelf is widest.

[42] The K_1 energy flux is about an order of magnitude weaker than M_2 and directed equatorward in the deep ocean. The equatorward flux in our model solutions is part of the western side of the CCW energy path around the North Atlantic Ocean. Energy arrives onto the Blake Plateau from the north and proceeds through the Florida Straits and into the Gulf of Mexico. Although the flux on the shelf is very weak, it is poleward and enters the SAB shelf from the south.

[43] The distribution of the M_2 and K_1 dissipation rates ϵ is shown (as $\log_{10}\epsilon$) in Figure 9. There is increased dissipation in the estuary solution, relative to the no-estuary solutions, because of the increased tidal velocities in the inlet region as well as the change in the phase relationship between the velocity and elevation. This latter part is because $\epsilon \sim \nabla \cdot \mathbf{F}$, since the work term is negligible. The dissipation rate (due only to bottom friction in our solutions) over a tidal period T in the SAB is diagnosed from [*Taylor*, 1919]:

$$\epsilon = \frac{\kappa\rho}{T}\int_T \left[u(t)^2 + v(t)^2\right]^{\frac{3}{2}} dt$$

where T is the tidal period, $u(t)$, $v(t)$ are the depth-averaged velocity components evaluated at time t, κ is the bottom friction coefficient, and ρ is a reference density. The units of ϵ are W m^{-2}.

[44] For both frequencies, the highest rates on the shelf occur in the midshelf region where the shelf is widest and where the tidal velocities are largest. Relative to the deep ocean, there is increased dissipation on the Blake Plateau and also enhanced dissipation around the shallow Bahama Banks. For M_2, the estuary solution has maximum midshelf dissipation rates in excess of $10^{-1.5}$ ($\sim$0.03) W m^{-2} seaward of the ETIC. This compares to maximum midshelf rates of less than $10^{-1.5}$ W m^{-2} in the no-estuary solution. The M_2 dissipation rate in a portion of the ETIC is shown in Figure 10. The dissipation rate reaches $10^{-0.3}$ ($\sim$0.5) W m^{-2} in the tidal inlets. This increase, due to the presence of the ETIC, is not as large in the K_1 solutions. The rate is generally four orders of magnitude smaller than that for M_2.

[45] Integrals of the dissipation rate are computed as $T_\epsilon = \int\int_A \epsilon dA$ where the area of integration A is the SAB shelf region out to the 100-m isobath and including the ETIC. The dissipation in the entire SAB at the M_2 frequency sums to 1.6 GW for the estuary solution, and to 0.72 GW for the no-estuary solution. In the ETIC region alone (defined here

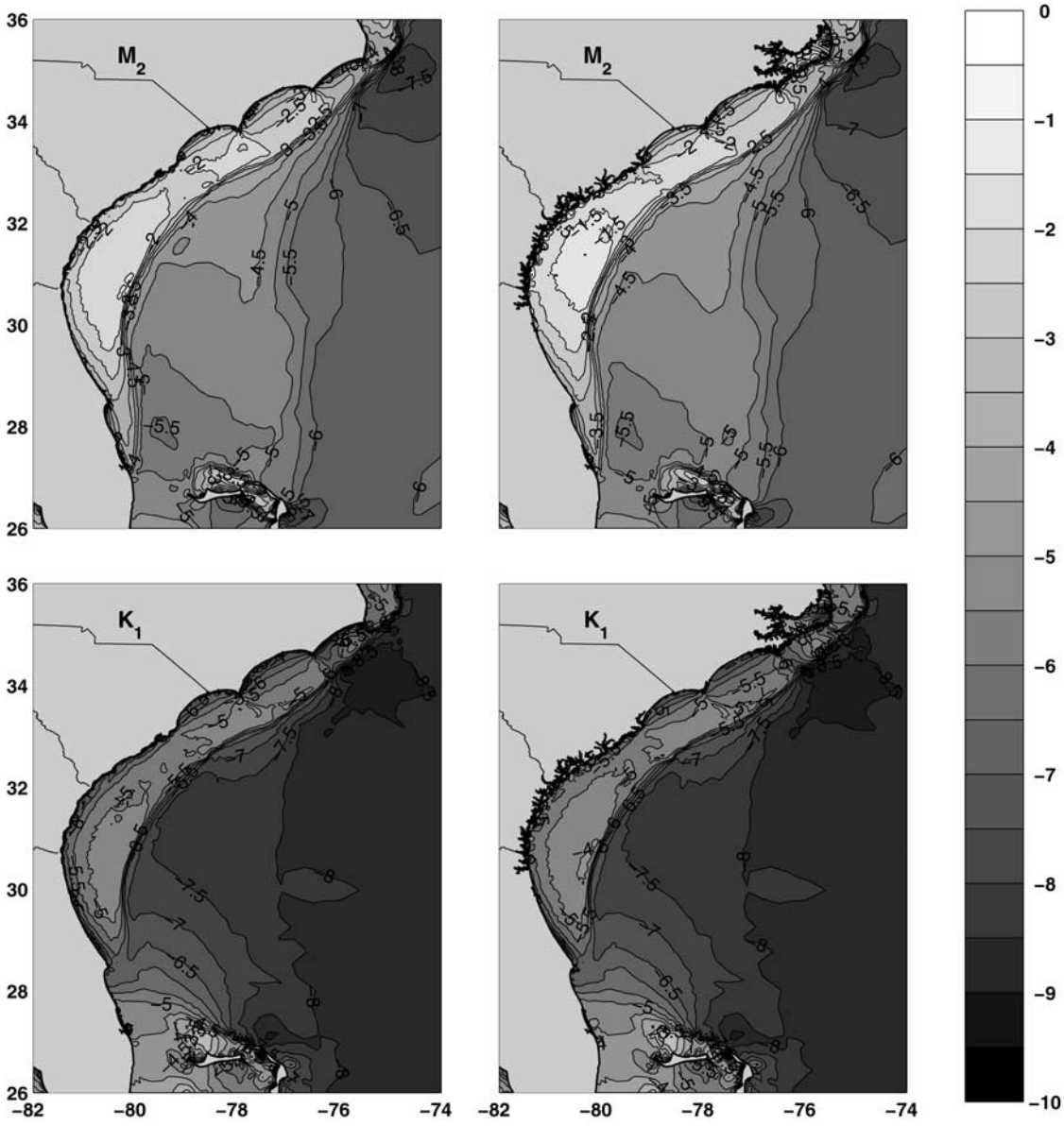

Figure 9. Diagnosed M_2 and K_1 energy dissipation per unit area (ϵ) for tidal solutions without the ETIC (left) and with ETIC (right). The scalar shown is $\log_{10}\epsilon$. The total dissipation of M_2 tidal energy over the tidal period in the SAB is 1.6 GW in the estuary solution and 0.72 GW in the no-estuary solution. The total M_2 dissipation in the ETIC is 0.42 GW, or 25% of the estuary solution dissipation in the SAB. See color version of this figure at back of this issue.

as shoreward of the 10-m isobath), the total dissipation is about 0.42 GW, or about 25% of the SAB dissipation. Thus, the ETIC in the SAB not only dissipates about one quarter of the energy dissipated in the SAB, but it also causes a two-fold increase in the SAB dissipation over the model solution that does not include the ETIC.

4. Discussion

[46] There is generally good agreement between the observations and model solution that includes the representation of the ETIC. Cross-shelf elevation amplification of the semidiurnal tides, particularly M_2, is significant. Relative to the deep ocean value of 0.45 m [*Pearson*, 1975], the coastal amplification is a factor of 2.5 at the widest part of the shelf. Most of the amplification occurs on the continental shelf, where the shelf break amplitude is uniformly 0.50 m to 0.55 m. The latest M_2 phase observed on the shelf proper is about 17° along the Georgia/Florida border. Previously published solutions [*Chen et al.*, 1999] report a largest nearshore phase of 30°.

[47] The K_1 tidal amplitude, however, increases from the deep value of 0.10 m to about 0.12 m. K_1 tidal velocities are about 0.01 to 0.02 m s^{-1}, roughly the same as that reported for the lower MAB [*Lentz et al.*, 2001], and smaller by a factor of 2 than K_1 velocities along the west Florida shelf [*He and Weisberg*, 2002]. The disagreement in the K_1 velocity inclination and phase at the stations R5 and GR

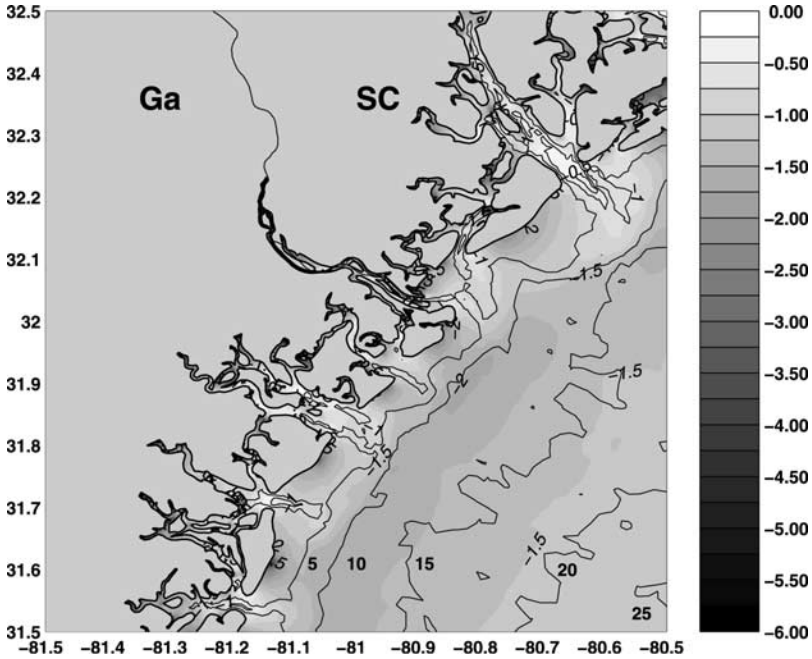

Figure 10. Diagnosed M_2 energy dissipation per unit area in a part of the ETIC. The scalar shown is $\log_{10}\epsilon$. The 5, 10, 15, 20, and 25-m isobaths are included. See color version of this figure at back of this issue.

is large. Inference of P_1 from K_1 is not the source of the discrepancy. The model solutions are smooth in this regard. We note that the O_1 ellipse parameters are also variable, and that the largest diurnal errors occur for stations with the shortest record lengths. Additionally, the diurnal tidal periods are close to the inertial period in the middle SAB region, and inertial motions generated by weather-related forcing could be contaminating the tidal signal. *Lentz et al.* [2001] indicate that the K_1 along-shelf velocity component is influenced by diurnal winds on the southern MAB shelf.

[48] The differences in the model solutions for M_2 indicate that the energy dissipated in the ETIC (in the estuary solution) is provided by a larger-scale adjustment between the water level and velocity field, relative to the no-estuary solution. Since the M_2 amplification ratio is greater than one and the estuary solution lags the no-estuary solution on the shelf in front of the ETIC (Figure 6), this implies that high water in the SAB is higher and occurs later in the model solution that resolves the ETIC.

[49] Midlatitude semidiurnal tides on wide shelves experience amplification because they can propagate cross-shelf as inertia-gravity waves [*Clarke and Battisti*, 1981; *Clarke*, 1991]. As the waves approach the coastal wall, they reflect and constructively interfere. Since the ETIC provides a modification to the ''reflective'' characteristics of the landward boundary, the reflection of semidiurnal tides is substantially affected. Diurnal tides do not propagate as inertia-gravity waves at midlatitudes and are not as affected by the alteration of the landward boundary region.

[50] The diagnosis of this difference in solutions is shown in Figure 11. The energy flux vector (F_x, F_y) (equation (2)) is computed from both solutions, and the vector differences are plotted. For both M_2 and K_1, this indicates that there must be additional energy supplied to the estuary region, and this energy comes from offshelf, almost directly cross-shelf. The magnitude of the K_1 flux difference is about two orders of magnitude smaller than that for M_2. There is also an increased energy flux toward the Pamlico sound area of the North Carolina coast. Since the elevation on the open boundary at 60°W is identical in both solutions (and therefore so is the elevation gradient along the boundary), the pressure work done on the open boundary is the same. However, the elevation gradient normal to the open boundary is not (cannot be) specified, so the velocity field at the boundary adjusts in response to the increased dissipation in the ETIC. (The K_1 difference shows a confused pattern off the North Carolina coast. This artifact results from the differences in a region of rapid phase changes between the two solutions.)

[51] The elevation and velocity adjustments in the estuary-resolving solution thus conspire to provide this additional energy to the estuaries. Both the elevation and velocity phase adjust over a large area, indicating that the character of the tidal wave becomes more progressive, resulting in a larger energy flux shoreward. Tidal energy is transported toward the tidal inlet and estuary regions, where this energy is ultimately dissipated. Since the reflection of the tide is not as large when the boundary is perforated with holes (which provide large energy sinks), a more progressive wave results that provides more energy.

[52] The poleward M_2 energy flux (Figure 8) is a branch of the larger basin-wide poleward semidiurnal flux that transports energy from the South Atlantic Ocean into the North Atlantic. According to energy budget analyses of global tidal model solutions [*Kantha et al.*, 1995; *Lyard and Le Provost*, 1997; *Le Provost and Lyard*, 1997], the North Atlantic Ocean dissipates more energy than is input into it through direct lunar and solar gravitational loading, and thus a flux of energy is required into the North Atlantic. The only source for this needed additional energy is flux from the

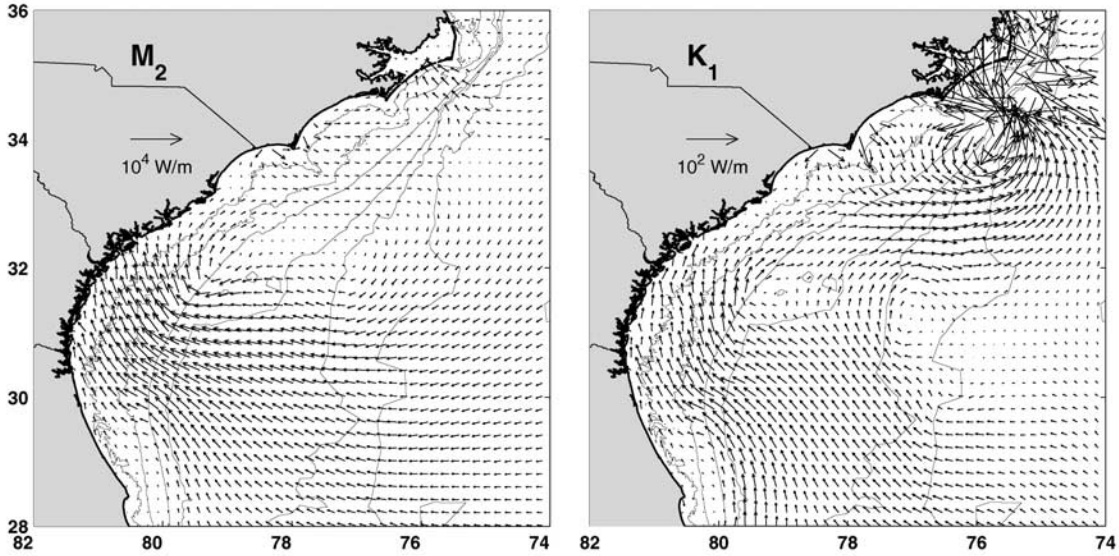

Figure 11. M_2 and K_1 energy flux difference between the tidal solutions with and without inclusion of the ETIC in the SAB. The bathymetry is shown with the light lines (20, 35, 60, 200, 1000, 3000, and 5000-m isobaths).

South Atlantic through the equatorial region (see Figure 1 in *Kantha et al.* [1995] and Figure 2 in *Lyard and Le Provost* [1997]). This energy path splits in two: an eastern branch delivers tidal energy to the northwest European shelf and Arctic Ocean, and a smaller branch feeds into the Gulf of Maine, which is seen on the eastern side of our domain.

[53] The thick dashed line in Figure 8 marks the zone along which the flux magnitude is minimum (but not zero). Locally, this implies that the wave character is more standing (water level and depth averaged velocity in quadrature) than progressive, or that high water occurs at nearly the same time as minimum current speed. Although the energy flux on the SAB shelf is poleward, the water level phase and velocity phase are nearly in quadrature ($\sim$0° and $\sim$270°) throughout the SAB, which indicates that the semidiurnal tides are generally standing in nature; the relative phase difference between velocity and elevation is near, but not exactly, one quarter period. The elevation and velocity magnitudes are also much larger on the shelf than in deep water where the elevation and velocity are smaller but the flux is larger (due to a smaller phase difference and large water column depths).

[54] The North Atlantic Ocean appears to have an excess of K_1 energy input, and a flux occurs into the South Atlantic basin (see Figure 1 in *Kantha et al.* [1995]). The eastern side of this equatorward energy flux is seen in our solutions. On the SAB shelf, K_1 has a more progressive character than does M_2, since elevation and velocity phases are 185°–190° and 110°–130°, respectively.

[55] The estuary solution exhibits an increase in M_2 elevation and velocity amplitudes as well as elevation and velocity phase adjustments, of which the energy flux and dissipation are only diagnostics. The increase in the elevation amplitude in estuary solution, compared to the no-estuary solution, is contrary to the expectation that a head loss (elevation decrease) usually occurs in a more dissipative environment. We are investigating this issue separately. However, the mechanism is not clear.

[56] The drag coefficient used in this study (C_d = 0.003) is slightly higher than the more typical value used in vertically integrated model studies of tides (C_d = 0.0025). The higher value gives a better fit to observations throughout the entire model domain. The SAB coastal M_2 water levels are slightly higher and earlier in a set of model solutions (with and without the ETIC) computed with C_d = 0.0025. However, the solution without the ETIC still exhibits a much larger overall error compared to the solution with the ETIC. The reduced drag coefficient does not account for the error between the solution without the ETIC and the observations. Additionally, the M_2 amplification ratio and phase difference is not qualitatively affected by the lower drag coefficient. K_1 is not affected within the uncertainty of the observations.

[57] The tidal energy analysis presented above focuses on the individual tidal constituents M_2 and K_1. Some of the M_2 energy transported onto a continental shelf is transfered into nonlinear, shallow-water overtides, primarily M_4 and M_6. These constituents are locally generated through the interaction of strong bathymetric gradients, nonlinear bottom friction, and advective accelerations. In the region of the tidal inlets, these harmonics can be large and contribute to the total energy budget for M_2. We have not presented a formal energy budget for the SAB; this is the subject of a future communication. This will include some sensitivity of energy dissipation and flux differences over the spring-neap cycle. The elevation range at spring tides is twice that during neap tides, which implies that the tidal currents are also twice as large. The cubic nature of energy dissipation then implies a factor of 8 difference between spring and neap dissipation rates.

5. Conclusion

[58] This study presents an analysis of tidal water level and ADCP data in the South Atlantic Bight. Harmonic analysis of the observations confirms previously determined

rankings of the principal tidal contributions to elevation and depth-averaged current variability on the SAB shelf. These constituents are M_2, N_2, S_2, K_1 and O_1 for both water level and currents. Additionally, we have conducted numerical simulations using a finite element shallow-water model that includes a first-order representation of the estuary/tidal inlet complex along the Georgia/South Carolina coast. It has been shown that numerical solutions for the M_2 tide in the nearshore, inner shelf, and midshelf zones are sensitive to the inclusion of the ETIC. Diurnal tides are less sensitive. This substantially affects model skill for the semidiurnal tides.

[59] The model solutions along the shelf break of the M_2 tidal elevation amplitude and phase are consistent with basin-scale tidal model results. Inclusion of the ETIC along the Georgia/South Carolina coast fundamentally modifies the nearshore character of computed tidal solutions and decreases the rms error of semidiurnal tidal components for estuary and shelf stations to levels consistent with deep ocean errors. We expect that further improvements will be achieved with more detailed resolution of the coastal region as well as model solutions that include flooding and dewatering, an important process that we have not addressed in this effort. Additional improvements may be obtained by using more recent global tidal models for the open-water boundary conditions (e.g., the FES99 solutions in *Lefèvre et al.* [2002]).

[60] These results demonstrate that semidiurnal tidal solutions (particularly M_2) are sensitive to the representation of complex, highly dissipative geometries. Both the cross-shelf amplification and phase lag are affected. Diurnal tides are essentially unaffected. In light of previous tidal solutions in the South Atlantic Bight that do not include the estuary/tidal inlet complex, it appears incorrect to compare those solutions with observations that either are not geometrically located within the domain, or in close proximity to the coastal region.

[61] **Acknowledgments.** The authors thank Luke Stearns and Mike Muglia for processing the ADCP data and Karen Pehrson-Edwards for comments on the manuscript. We also thank two anonymous reviewers, whose comments greatly improved the manuscript. We thank Jack Blanton for providing data from stations D86, D87, and SNLT. This research was supported under NOPP grants NAG13-00041 and N00014-98-1-0786.

References

Blanton, B. O. (2003), Towards operational modeling in the South Atlantic Bight, dissertation, Univ. of N. C., Chapel Hill.

Carrère, L., C. L. Provost, and F. Lyard (2004), On the statistical stability of the M_2 barotropic and baroclinic tidal characteristics from along-track TOPEX/Poseidon satellite altimetry analysis, *J. Geophys. Res.*, *109*, C03033, doi:10.1029/2003JC001873.

Chen, C., L. Zheng, and J. O. Blanton (1999), Physical processes controlling the formation, evolution, and perturbation of the low-salinity front in the inner shelf off the southeastern United States: A modeling study, *J. Geophys. Res.*, *104*(C1), 1259–1288.

Clarke, A. J. (1991), The dynamics of barotropic tides over the continental shelf and slope (review), in *Tidal Hydrodynamics*, edited by B. Parker, pp. 79–108, John Wiley, Hoboken, N. J.

Clarke, A. J., and D. S. Battisti (1981), The effect of continental shelves on tides, *Deep Sea Res.*, *28*, 665–682.

Davies, A. M., and C. M. Kwong (2000), Tidal energy fluxes and dissipation on the European continental shelf, *J. Geophys. Res.*, *105*(C9), 21,969–21,989.

Egbert, G. D., and R. Ray (2000), Significant dissipation of tidal energy in the deep ocean inferred from satellite altimeter data, *Nature*, *405*, 775–778.

Foreman, M. G. G., and R. E. Thomson (1997), Three-dimensional model simulations of tides and buoyancy currents along the west coast of Vancouver Island, *J. Phys. Oceanogr.*, *27*, 1300–1325.

Foreman, M. G. G., R. A. Walters, R. F. Henry, C. P. Keller, and A. G. Dolling (1995), A tidal model for eastern Juan de Fuca Strait and the southern Strait of Georgia, *J. Geophys. Res.*, *100*(C1), 721–740.

Glorioso, P., and R. Flather (1997), The Patagonian Shelf tides, *Progr. Oceanogr.*, *40*, 263–283, doi:10.1016/S0079-6611(98)00004-4.

He, R., and R. H. Weisberg (2002), Tides on the West Florida Shelf, *J. Phys. Oceanogr.*, *32*, 3455–3473.

Kang, S. K., J.-Y. Chung, S.-R. Lee, and K.-D. Yum (1995), Seasonal variability of the M_2 tide in the seas adjacent to Korea, *Cont. Shelf Res.*, *15*(9), 1087–1113.

Kang, S. K., M. G. G. Foreman, W. R. Crawford, and J. Y. Cherniawsky (2000), Numerical modeling of internal tide generation along the Hawaiian Ridge, *J. Phys. Oceanogr.*, *30*, 1083–1098.

Kang, S. K., M. G. G. Foreman, H.-J. Lie, J.-H. Lee, J. Cherniawsky, and K.-D. Yum (2002), Two-layer tidal modeling of the Yellow and East China Seas with application to seasonal variability of the M_2 tide, *J. Geophys. Res.*, *107*(C3), 3020, doi:10.1029/2001JC000838.

Kantha, L. H. (1995), Barotropic tides in the global ocean from a nonlinear tidal model assimilating altimetric tides: 1. Model description and results, *J. Geophys. Res.*, *100*(C12), 25,283–25,308.

Kantha, L. H., and C. Tierney (1997), Global baroclinic tides, *Progr. Oceanogr.*, *40*, 163–178.

Kantha, L. H., C. Tierney, J. W. Lopez, S. D. Desai, M. E. Parke, and L. Drexler (1995), Barotropic tides in the global ocean from a nonlinear tidal model assimilating altimetric tides: 2. Altimetric and geophysical implications, *J. Geophys. Res.*, *100*(C12), 25,309–25,317.

Lee, T. N., and D. Brooks (1979), Initial observations of current, temperature, and coastal sea level response to atmospheric and Gulf Stream forcing, *Geophys. Res. Lett.*, *6*, 321–324.

Lefèvre, F., F. Lyard, and C. Le Provost (2002), FES99: A global tide finite element solution assimilating tide gauge and altimetric information, *J. Atmos. Oceanic Technol.*, *19*, 1345–1356.

Lentz, S., M. Carr, and T. H. C. Herbers (2001), Barotropic tides on the North Carolina shelf, *J. Phys. Oceanogr.*, *31*, 1843–1859.

Le Provost, C., and F. H. Lyard (1997), Energetics of the M_2 barotropic ocean tides: An estimate of bottom friction dissipation from a hydrodynamic model, *Progr. Oceanogr.*, *40*, 37–52.

Le Provost, C., F. H. Lyard, J.-M. Molines, M.-L. Genco, and F. Rabilloud (1998), A hydrodynamic ocean tide model improved by assimilating a satellite altimeter-derived data set, *J. Geophys. Res.*, *103*(C3), 5513–5529.

Luettich, R. A., J. J. Westerink, and N. W. Scheffner (1992), ADCIRC: An advanced three-dimensional circulation model for shelves, coasts and estuaries; report 1: Theory and methodology of ADCIRC-2DDI and ADCIRC-3DL, *Tech. Rep. DRP-92-6*, Coastal Eng. Res. Cent., U.S. Army Eng. Waterw. Exp. Stn., Vicksburg, Miss.

Luettich, R., J. Hench, C. Fulcher, F. Werner, B. Blanton, and J. Churchill (1999), Barotropic tidal and wind driven larvae transport in the vicinity of a barrier island inlet, *J. Fish. Oceanogr.*, *8*(2), suppl. 2, 190–209.

Lyard, F. H., and C. Le Provost (1997), Energy budget of the tidal hydrodynamic model FES94.1, *Geophys. Res. Lett.*, *24*, 687–690.

Lynch, D. R., and C. E. Naimie (1993), The M_2 tide and its residual on the outer banks of the Gulf of Maine, *J. Phys. Oceanogr.*, *23*, 2222–2253.

Lynch, D., et al. (2001), Real-time data assimilative modeling on Georges Bank, *Oceanography*, *14*(1), 65–77.

Lynch, D., K. Smith, B. Blanton, F. Werner, and R. Luettich (2004), Forecasting the coastal ocean: Resolution, tide and operational data in the South Atlantic Bight, *J. Atmos. Oceanic Technol.*, *21*(7), 1074–1085.

Mofjeld, H. (1976), Tidal currents, in *Marine Sediment Transport and Environmental Management*, edited by D. J. Stanley and D. J. P. Swift, pp. 53–64, John Wiley, Hoboken, N. J.

Moody, J. A., B. Butman, R. C. Beardsley, W. S. Brown, D. A. Mayer, H. O. Mofjeld, B. Petrie, S. Ramp, P. Smith, and W. R. Wright (1984), Atlas of tidal elevation and current observations on the northeast American continental shelf and slope, *U.S. Geol. Surv.*, *1611*.

Mukai, A., J. Westerink, R. Luettich, and D. Mark (2002), Eastcoast 2001: A tidal constituent database for the western North Atlantic, Gulf of Mexico and Caribbean Sea, *Tech. Rep. ERDC/CHL TR-02-24*, Coastal and Hydraul. Lab., U.S. Army Eng. Res. and Dev. Cent., Vicksburg, Miss.

Munk, W. (1997), Once again: Once again—Tidal friction, *Progr. Oceanogr.*, *40*, 7–35.

Naimie, C. E., J. W. Loder, and D. R. Lynch (1994), Seasonal variation of the three-dimensional residual circulation on Georges Bank, *J. Geophys. Res.*, *99*(C8), 15,967–15,989.

Pawlowicz, R., B. Beardsley, and S. Lentz (2002), Classical tidal harmonic analysis including error estimates in MATLAB using TTIDE, *Comput. Geosci.*, *28*, 929–937.

Pearson, C. (1975), Deep-sea tide observations off the southeastern United States, *Tech. Rep. NOAA Tech. Memo. 17*, 16 pp., Natl. Oceanic and Atmos. Admin., Rockville, Md.

Pietrafesa, L. J., J. O. Blanton, J. D. Wang, V. H. Kourafalou, T. N. Lee, and K. A. Bush (1985), The tidal regime in the South Atlantic Bights, in *Oceanography of the Southeastern U.S. Continental Shelf*, edited by L. P. Atkinson, D. W. Menzel, and K. A. Bush, pp. 63–76, AGU, Washington, D. C.

Prandle, D. (1982), The vertical structure of tidal currents, *Geophys. Astrophys. Fluid Dyn.*, *22*, 29–49.

Pugh, D. T. (1987), *Tides, Surges, and Mean Sea Level: A Handbook for Scientists and Engineers*, 472 pp., John Wiley, Hoboken, N. J.

Ray, R. D., and G. T. Mitchum (1997), Surface manifestation of internal tides generated near Hawaii, *Progr. Oceanogr.*, *40*, 135–162.

Redfield, A. (1958), The influence of the continental shelf on the tides of the Atlantic coast of the United States, *J. Mar. Res.*, *1492*, 432–448.

Ryan, J., and J. Yoder (1996), Long-term mean and event–related pigment distributions during the unstratified period in South Atlantic Bight outer margin middle shelf waters, *Cont. Shelf Res.*, *16*, 1165–1183.

Seim, H. (2000), Implementation of the South Atlantic Bight Synoptic Offshore Observational Network, *Oceanography*, *13*, 18–23.

Shanks, A. (1988), Further support for the hypothesis that internal waves can cause shoreward transport of larval invertebrates and fish, *Fish. Bull.*, *86*, 703–714.

Taylor, G. I. (1919), Tidal friction in the Irish Sea, *Philos. Trans. R. Soc. London*, *220*, 1–93.

Tebeau, P. A., and T. N. Lee (1979), Wind induced circulation on the Georgia shelf, *Tech. Rep. 79003*, 177 pp., Univ. of Miami, Miami, Fla.

Way, F. (1998), Hydrodynamic and water quality monitoring of the lower Savannah River estuary, July to September 1997, technical report, Ga. Ports Auth., Savannah.

Werner, F. E., J. O. Blanton, D. R. Lynch, and D. K. Savidge (1993), A numerical study of the continental shelf circulation of the U.S. South Atlantic Bight during the autumn of 1987, *Cont. Shelf Res.*, *13*(8/9), 871–997.

F. M. Bingham, Center for Marine Science, University of North Carolina at Wilmington, Wilmington, NC 28409, USA.

B. O. Blanton, R. A. Luettich Jr., H. E. Seim, and F. E. Werner, Department of Marine Sciences, University of North Carolina at Chapel Hill, Chapel Hill, NC 27599-3300, USA. (brian_blanton@unc.edu)

D. R. Lynch and K. W. Smith, Thayer School of Engineering, Dartmouth College, Hanover, NH 03755, USA.

G. Voulgaris, Department of Geological Sciences, University of South Carolina, Columbia, SC 29208, USA.

F. Way, Applied Technology and Management, Inc., P.O. Box 20336, Charleston, SC 29413-0336, USA.

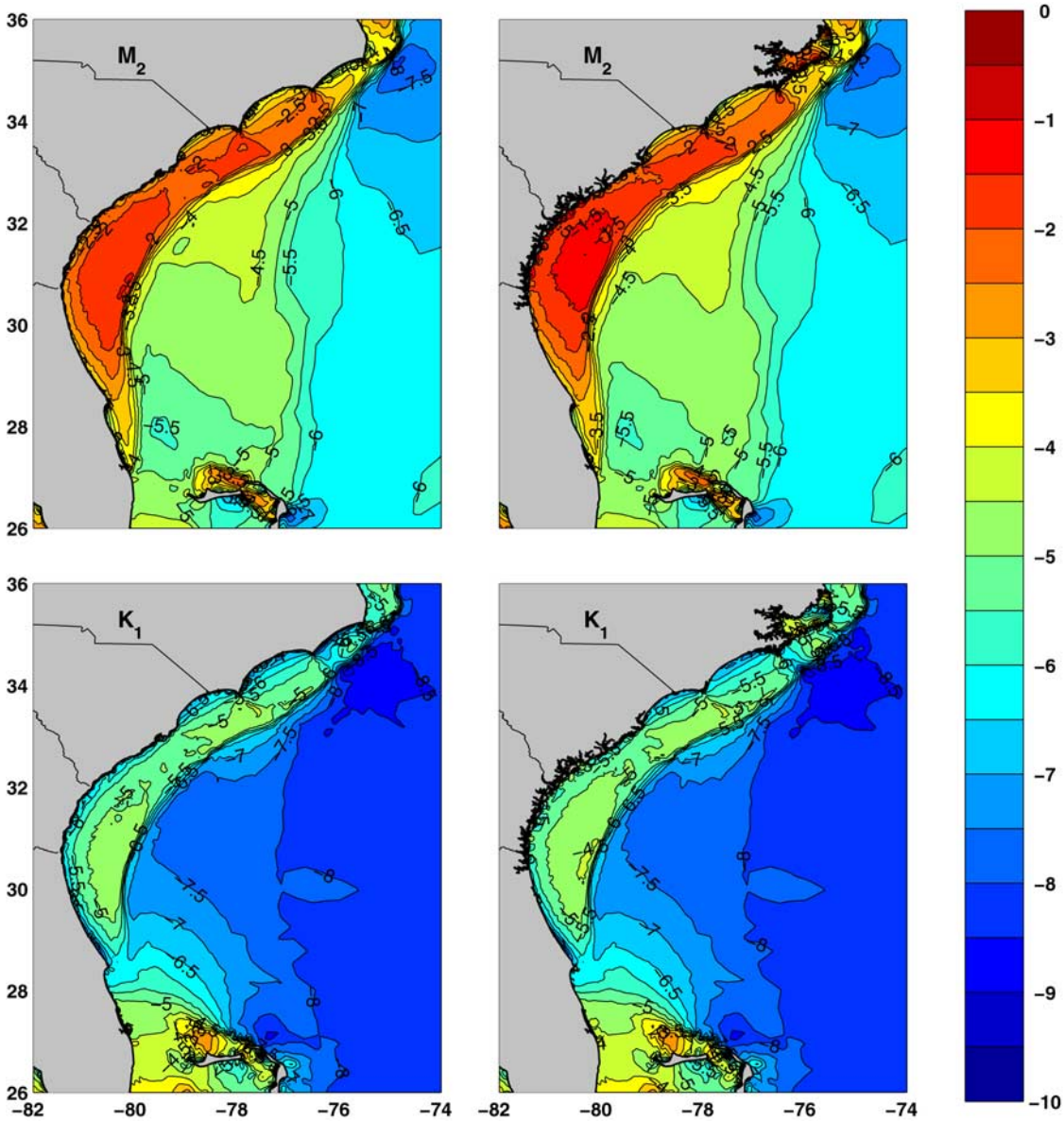

Figure 9. Diagnosed M_2 and K_1 energy dissipation per unit area (ϵ) for tidal solutions without the ETIC (left) and with ETIC (right). The scalar shown is $\log_{10}\epsilon$. The total dissipation of M_2 tidal energy over the tidal period in the SAB is 1.6 GW in the estuary solution and 0.72 GW in the no-estuary solution. The total M_2 dissipation in the ETIC is 0.42 GW, or 25% of the estuary solution dissipation in the SAB.

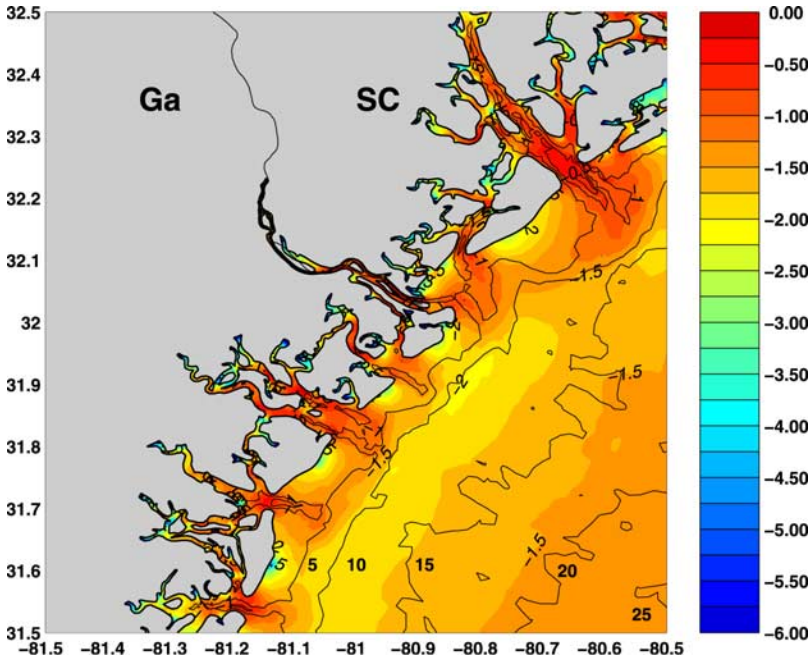

Figure 10. Diagnosed M_2 energy dissipation per unit area in a part of the ETIC. The scalar shown is $\log_{10}\epsilon$. The 5, 10, 15, 20, and 25-m isobaths are included.